

4-2020

## Interaction of High Aspect-Ratio Micro-Pillars with Wall Turbulence

Pratik Suhas Deshpande

Follow this and additional works at: <https://commons.erau.edu/edt>

 Part of the [Aerospace Engineering Commons](#)

---

This Thesis - Open Access is brought to you for free and open access by Scholarly Commons. It has been accepted for inclusion in Dissertations and Theses by an authorized administrator of Scholarly Commons. For more information, please contact [commons@erau.edu](mailto:commons@erau.edu).

INTERACTION OF HIGH ASPECT-RATIO MICRO-PILLARS WITH WALL  
TURBULENCE

By

Pratik Suhas Deshpande

A Thesis Submitted to the Faculty of Embry-Riddle Aeronautical University  
In Partial Fulfillment of the Requirements for the Degree of  
Master of Science in Aerospace Engineering

April 2020

Embry-Riddle Aeronautical University

Daytona Beach, Florida

INTERACTION OF HIGH ASPECT-RATIO MICRO-PILLARS WITH WALL  
TURBULENCE

By

Pratik Deshpande

This Thesis was prepared under the direction of the candidate's Committee Chair, Dr. Ebenezer Gnanamanickam, Department of Aerospace Engineering, and has been approved by the members of the Thesis Committee. It was submitted to the Office of the Senior Vice President for Academic Affairs and Provost, and was accepted in partial fulfillment of the requirements for the Degree of Master of Science in Aerospace Engineering.

THESIS COMMITTEE




---

Chairman, Dr. Ebenezer Gnanamanickam



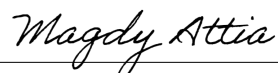

---

Member, Dr. Reda Mankbadi



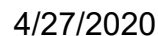

---

Member, Dr. Mark Ricklick




---

Graduate Program Coordinator,  
Dr. Magdy Attia



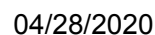

---

Date




---

Dean of College of Engineering,  
Dr. Maj Mirmirani



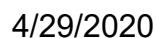

---

Date




---

Associate Provost of Academic Support,  
Dr. Christopher Grant




---

Date

## ACKNOWLEDGEMENTS

I'd like to thank Embry Riddle Aeronautical University for giving the opportunity to work on this thesis. It was a learning experience that exposed me to the world of research. I gratefully acknowledge the support of my parents, Suhas Deshpande and Rani Deshpande, without whom I would not be here. This thesis is the result of the constant support I have received from multiple people.

First and foremost, I extend my grateful thanks to my advisor, Dr. Ebenezer Gnanamanickam, for his continued guidance and support throughout my thesis. I have learnt a lot about research under his tutelage and the values he instilled in me will help me in my future research pursuits.

I would also like to thank the members of my committee, Dr. Reda Mankabadi and Dr. Mark Ricklick, for their guidance and support. Their feedback helped me improve my thesis. A very special thanks to Bill Russo for his help in my experimental set-up.

I am also thankful to Dr. Zheng Zhang for his help in my initial stages of the experiment. He helped me understand the workings of the wind tunnel lab and got me started with experimental data collection. I also thank Sravan Artham and Dr. Shibani Bhatt for my initiation into the world of experimental aerodynamics research.

Finally, I would like to thank my friends: Farhan, Sreeja, Harsh, Varad and Omkar among others. Their constant support has been invaluable to me.

## ABSTRACT

An experimental study of the interaction between hairy structures modeled as high-aspect ratio micro-pillars (HAMuP) and wall turbulence is presented. Micro-pillars are elastic, hair-like micro-structures which have been inspired by naturally occurring examples like lateral line sensors in fish and air flow sensors in bats. The objective of this thesis was two fold: to develop a manufacturing process for consistent production of HAMuP arrays, and to conduct a study focusing on the interaction of HAMuP arrays with wall turbulence. Hot-wire anemometry measurements were carried out in two different experimental facilities at three different streamwise locations to describe the interaction between the HAMuP array and the wall-turbulence. There is a shift of the laminar sub-layer away from the wall indicated by a shift in the turbulent-intensity peak in the inner region of the flow over HAMuP array. The energy spectra also reveals a shift of the energetic structures away from the wall. Measurements taken downstream of the HAMuP array point to a damping of the energetic structures in the flow over the HAMuP array. The amplitude modulation coefficient is increased in the near-wall region which points to a possible mechanism by which the naturally occurring micro-pillars detect oncoming predators. A parametric approach was adopted to further study the effect of HAMuP arrays on turbulent boundary layer. The parameter study also reveals that a decrease in elastic modulus may lead to a decrease in the amount of energy the HAMuP arrays can extract from the flow. Also, increasing the height of the pillars might increase the potential elastic energy they can store but there is also a potential increase in the form drag due to the micro-pillars.

## TABLE OF CONTENTS

ACKNOWLEDEMENTS . . . . .	iii
ABSTRACT . . . . .	iv
LIST OF FIGURES . . . . .	vi
LIST OF TABLES . . . . .	x
ABBREVIATIONS . . . . .	xi
NOMENCLATURE . . . . .	xii
1. Introduction . . . . .	1
2. Background . . . . .	4
2.1. Turbulent Flow over Smooth Walls . . . . .	4
2.1.1. Energy Cascade and Near-Wall Production Cycle . . . . .	6
2.2. Turbulent Flow over Rough Walls . . . . .	7
2.2.1. Effect of Roughness on The Mean Flow . . . . .	9
2.3. Turbulent Flow over Flexible Roughness Elements . . . . .	15
3. Description of the Experiment . . . . .	19
3.1. HAMuP Manufacturing Setup . . . . .	19
3.1.1. Manufacturing the Micro-pillar Mold . . . . .	19
3.1.2. Casting the HAMuP Array . . . . .	20
3.1.3. HAMuP Array . . . . .	21
3.2. Hot-wire Anemometry . . . . .	22
4. Results and Discussion . . . . .	25
4.1. Interaction of HAMuP Array with Wall Turbulence . . . . .	25
4.2. Effect of Change in Elastic Modulus on HAMuP Performance . . . . .	34
4.3. Effect of Micro-Pillar Height on HAMuP Performance . . . . .	38
5. Conclusion and Future Work . . . . .	41
REFERENCES . . . . .	43

## LIST OF FIGURES

Figure	Page	
1.1	Examples of Micro-pillars in nature: a. line sensors in fish function as sensors helping them navigate, find prey and evade predators, b. sensory hairs in bats serve as airflow sensors that help them avoid stall and c. an array of sensory hairs help crickets create an acoustic image of their surroundings (Bechert, Bruse, Hage, & Meyer, 2000; Marshall et al., 2015; Tao & Yu, 2012) .....	1
2.1	Law of the wall: The velocity profile is defined for different regions in the flow. In the viscous sub-layer, the flow is dominated by viscous scales only. In the log-layer, inertial scales are dominant. The buffer layer is where both inertial and viscous forces dominate (Mehta, Thota Radhakrishnan, & Clemens, 2018).....	5
2.2	The figure illustrates the energy cascade. Energy is transferred from the energetic containing scales to the dissipative scales (Makris, Memos, & Krestenitis, 2016).....	7
2.3	a. “d-type grooves in the surface. It has been hypothesized that the deep grooves sustain stable re-circulation vortices that isolate the roughness from the mean flow. b. k-type grooves in the surface have a width greater than 3-4 k which results in a re-circulation bubble that reattaches ahead of the next groove exposing the roughness to the mean flow” (Jiménez, 2004, p.181). .....	9
2.4	The figure shows Pre-multiplied spectral density $k_x E_{uu}$ , as a function of the stream-wise wavelength $\lambda_x = 2\pi/k_x$ , and of the wall distance — smooth wall, - - - - , rough wall (Jiménez, 2004).....	10
2.5	Integral length scales of the velocity components as a function of distance from the wall. The filled square is the integral length scale of the radial velocity component in the streamwise direction ( $L_{22}$ ). The unfilled square is the integral length scale of the streamwise velocity component in the streamwise direction ( $L_{11}$ ). -----, rough pipe, - - - - , smooth pipe (Sabot, Saleh, & Comte-Bellot, 1977).....	11
2.6	Pre-multiplied energy spectra for rough and smooth cases.....	12
2.7	Example sketch of riblet geometry. The riblet film had a height of 0.114mm and was studied under both sub-sonic and supersonic conditions (Vishwanath, 2002).....	13

Figure	Page
2.8 Sketch of converging-diverging riblet geometry used by Nugroho, Hutchins, and Monty (2013). The height of the riblets was 0.5 mm and the spacing was 0.675 mm (Nugroho et al., 2013).....	13
2.9 Microscopic features of bird flight feathers used by Chen, Rao, Shang, Zhang, and Hagiwara (2014) to design bio-inspired herringbone riblets. The bio-inspired riblets reduced the drag by about 17-21% (Chen et al., 2014).....	14
2.10 Schematic of the experimental setup (Toloui, Abraham, & Hong, 2019).....	15
2.11 Reynolds stresses for rigid and flexible roughness elements (Toloui et al., 2019).....	16
2.12 Total Kinetic Energy for rigid and flexible roughness elements (Toloui et al., 2019).....	17
2.13 The figure shows the four k-type roughness bars used as dynamic roughness by Jacobi and McKeon (2011). Different hot wire measurement locations are also shown (Jacobi & McKeon, 2011).....	17
2.14 The figure illustrates a dense carpet of elastomeric micro-hairs of length 1mm arranged in a regular grid (60 by 30) (Brücker, 2011).....	18
3.1 Schematic of the CNC router used to punch holes in the wax sheet to create the micro-pillar molds.....	20
3.2 The vacuum chamber apparatus used for casting of micro-pillar arrays.....	21
3.3 A small section of the HAMuP array showing individual micro-pillars.....	21
3.4 Hot-wire measurement stations over the HAMuP array.....	22
3.5 Experimental facility 1: zero-pressure gradient wind tunnel. The measurements were carried out 6 ft from the sandpaper trip at the inlet.....	23
3.6 $C_p v x$ for the zero-pressure gradient wind tunnel measured at three different velocities. The $\Delta C_p$ was less than 0.01 for all the different velocities. Each port was separated by a distance of 6 inches.....	24
3.7 Experimental Set-up 2: 25 ft long Boundary Layer Wind Tunnel.....	24
4.1 Hot-wire measurement locations for data collection.....	25



Figure	Page	
4.2	The mean velocity profile $U$ for HAMuP array 1 in comparison with the velocity profile over a smooth wall. The red region represents the approximate height of the HAMuP array.....	26
4.3	The figure illustrates the turbulent intensity profiles for HAMuP array 1 in comparison with a smooth wall. Turbulence intensity for large and small scales in the flow is also shown. The red region represents the approximate height of the HAMuP array.....	27
4.4	The figure here presents the outer normalized, pre-multiplied, 1-d streamwise energy spectra, $k_x \phi_{xx}$ , for smooth wall and the HAMuP 1. The dotted line is the division between large scale and small scales. The red region represents the average height of the HAMuP array.....	28
4.5	The figure shows the amplitude modulation coefficient ( $R_{AM}$ ) for HAMuP array 1 in comparison with a smooth wall. The red region represents the approximate height of the HAMuP array.....	29
4.6	The figure shows the mean velocity profile for HAMuP array 1 in comparison with the smooth wall at location 2. The red region represents the approximate height of the HAMuP array.....	30
4.7	The figure shows the mean velocity profile for HAMuP array 1 in comparison with the smooth wall at location 2. The red region represents the approximate height of the HAMuP array.....	31
4.8	(a) The figure here presents the outer normalized, pre-multiplied, 1-d streamwise energy spectra, $k_x \phi_{xx}$ , for smooth wall and the HAMuP 1 at location 2. The dotted line is the division between large scale and small scales. The red region represents the average height of the HAMuP array. (b) $R_{AM}$ profiles for HAMuP 1 and smooth wall at location 2.....	32
4.9	(a) Mean velocity profile downstream of the HAMuP array (location 3). (b) Turbulent intensity profiles for HAMuP array at location 3. (c) The figure here presents the outer normalized, pre-multiplied, 1-d streamwise energy spectra, $k_x \phi_{xx}$ , for smooth wall and the micro-pillar array at location 3. The dotted line is the division between large scale and small scales. (d) $R_{AM}$ profiles for HAMuP 1 and smooth wall at location 3.....	33
4.10	The mean velocity profile of HAMuP array 1 and 2 along with the velocity profile over a smooth wall at location 1. The red region represents the approximate height of the HAMuP array.....	35

Figure	Page	
4.11	The figure illustrates the turbulent intensity profiles for HAMuP array 1 and 2 in comparison with a smooth wall. Turbulence intensity for large and small scales in the flow is also shown. The red region represents the approximate height of the HAMuP array.....	36
4.12	(a) The figure illustrates the outer normalized, pre-multiplied, 1-d streamwise energy spectra for HAMuP array 1 and 2 in comparison with a smooth wall at location 1. (b)The figure illustrates the $R_{AM}$ profiles for HAMuP array 1 and 2 in comparison with a smooth wall at location 1. The red region represents the approximate height of the HAMuP array.....	37
4.13	(a) The mean velocity profile for HAMuP array 1 and 3 is presented in comparison with a smooth wall at location 2. (b) The figure shows the turbulent-intensity profiles for HAMuP array 1 and 3 in comparison with a smooth wall. Turbulence-intensity for large and small scales in the flow is also shown. The red region presents the approximate height of HAMuP array 1.....	39
4.14	(a) The figure presents the outer normalized, pre-multiplied, 1-d streamwise energy spectra at location 2., (b) The figure shows the amplitude modulation coefficient, RAM, profiles for HAMuP 1 and 3. The red region represents the approximate height of HAMuP array 1.....	40

**LIST OF TABLES**

Table	Page
3.1 Table of parameters for different HAMuP arrays manufactured.....	22
4.1 Table of parameters for different HAMuP arrays manufactured.....	38

**ABBREVIATIONS**

DIH-PTV	Digital Inline Holographic particle tracking velocimetry
HAMuP	High-Aspect Ratio Micro-pillars
PIV	Particle Image Velocimetry
NASA	National Aeronautics and Space Administration
IOIM	Inner-Outer Interaction Model
HWA	Hot Wire Anemometry
TKE	Total Kinetic Energy
CNC	Computerized Numerical Control
CTA	Constant Temperature Anemometry
DAQ	Data Acquisition

## NOMENCLATURE

$E_p$	Elastic Modulus
$\Delta U^+$	Roughness function
$\delta$	Boundary Layer Thickness
$\delta_v$	Viscous length scale
$\varepsilon$	Roughness offset
$\kappa$	Von Kármán constant
$\nu$	Kinematic viscosity
$\Pi$	Coles wake factor
$\rho$	density
$C_p$	Coefficient of pressure
$E_L(u_s)$	Filtered large-scale envelope of the streamwise small-scale fluctuations
$EI$	Flexural rigidity
$I$	Moment of inertia
$k_s$	Equivalent roughness height
$k_s^+$	Roughness Reynolds number
$M$	Bending moment
$R_{AM}$	Amplitude Modulation Coefficient
$Re_\tau$	Friction Reynolds number
$U_\infty$	Mean free-stream velocity
$u_\tau$	Friction Velocity
$U_b$	Mean bulk velocity
$u_L$	large-scale component of the streamwise velocity fluctuations
$W$	Wake function
$y^+$	Wall units
$z$	Wall normal distance

## 1. Introduction

Turbulent wall bounded flows are commonly seen in aerodynamics such as the air flow over a wing, transportation of oil and water through pipelines, motion of ships, etc. Hence, their understanding is important to the goal of optimizing the performance of aerial vehicles by reducing skin friction drag, noise and vibration, etc. While flows over smooth surfaces are more prevalent in engineering applications, rough surfaces also play an important role in our world. Transportation of oil through pipelines which undergo fouling, bio-fouled surfaces of ships and vegetation canopies in the atmospheric boundary layer are some examples of flows over rough surfaces. Engineered rough surfaces may also have potential benefits. Riblets, inspired by the skin of the shark, are the most prominent of such surfaces and have been observed to serve the purposes of drag reduction (Bixler & Bhushan, 2013). A review of studies of flows over riblets (Vishwanath, 2002) observed upto 8 percent reduction in drag. However, recently the focus has shifted to the impact of flexible roughness elements on turbulent wall bounded flows. Flexible roughness elements offer a potential also for reduction of drag, noise and vibration (Toloui et al., 2019).

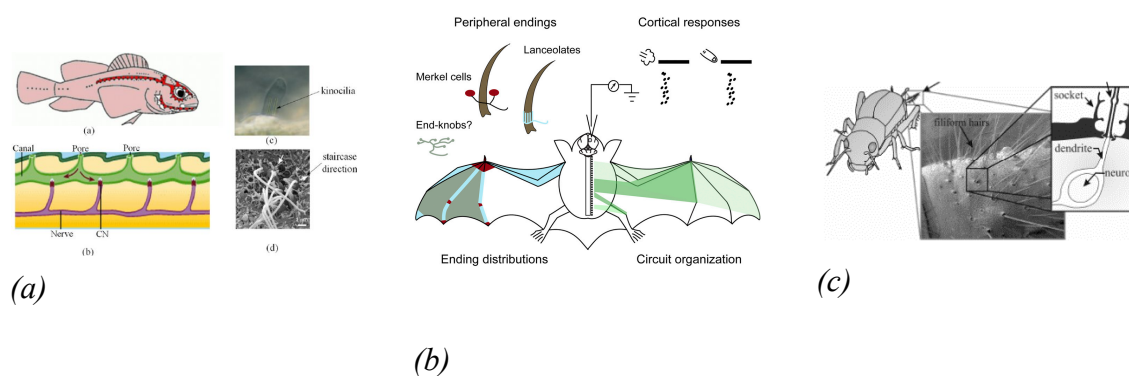


*Figure 1.1* Examples of Micro-pillars in nature: a. line sensors in fish function as sensors helping them navigate, find prey and evade predators, b. sensory hairs in bats serve as airflow sensors that help them avoid stall and c. an array of sensory hairs help crickets create an acoustic image of their surroundings (Bechert et al., 2000; Marshall et al., 2015; Tao & Yu, 2012).

High-aspect ratio micro-pillars (HAMuP), the subject of the present study, belong to

the flexible roughness family. HAMuP are hairlike structures inspired by naturally occurring examples like lateral line sensors in fish and airflow sensors in bats (see Figure 1.1) (Tao & Yu, 2012). Other examples of HAMuP include sensory hair on crickets and mosquitoes. Even grass and foliage in the earth's atmospheric boundary layer represent an example of HAMuP at work on a larger scale. From a functional standpoint, the airflow sensors used by bats detect the airflow over the wings and help avoid stall (Miller, 2005). Previous studies into the application of hairy surfaces have hypothesized that they may have a drag reducing benefit (Bechert et al., 2000). They also have been shown to function as thermal regulators in undersea creatures like otters (Bechert et al., 2000). Thus, engineered HAMuPs may have several practical applications which provides exciting new avenues for research.

Toloui et al. (2019) studied flexible micro-pillars and observed a reduction in turbulent kinetic energy and Reynolds' stresses when compared with rigid micro-pillars. More recently, Ch.Brucker investigated the interaction of near-wall turbulence with hairy surfaces in a turbulent boundary layer flow, along a flat plate in an oil channel, at  $Re = 1.2 \times 10^6$  (Brücker, 2011). It was hypothesized that the micro-hair carpet led to the stabilization of the near-wall streamwise velocity streaks which may point to a reduction in turbulent drag. Due to manufacturing constraints, small arrays have been used in these past studies. A much larger array is required to get a clearer understanding of the HAMuP-turbulence interaction, which is one of the goals of the present work.

Hence, from a physics standpoint, there is much that still remains unknown regarding the interaction of HAMuP with wall turbulence. This thesis is an attempt to answer a few of these unanswered questions. One of the issues researchers face in their study of micro-pillars is producing HAMuP arrays with consistency required for any rigorous investigation of its drag-reducing potential. Furthermore, to fully exploit HAMuP arrays for engineering benefit requires a deeper understanding of the HAMuP-turbulence interaction mechanism and its effect on various flow parameters. Thus, the objective of this thesis is two-fold: to develop a manufacturing process for consistent production of

High-Aspect Ratio Micropillars over large areas and to conduct a preliminary study focusing on the interaction of HAMuP arrays with wall turbulence using hot wire anemometry.

This thesis is organized as follows. Review of wall bounded flows and their interaction with different types of surfaces is presented in the next chapter. This is then followed by the chapter on the experimental approach which also discusses the HAMuP array production process. Results and a discussion on the conclusions to be drawn from the results obtained then follow.



## 2. Background

A background of the relevant material is presented in this chapter. First, smooth wall turbulence is considered. The different regions in the flow such as the sub-layer, overlap layer and outer layer are discussed along with relevant physics. This leads then to a survey of the impact of roughness elements on turbulent flows. Thereafter, a distinction between rigid and flexible roughness is made followed by a brief review of the work carried out on micro-pillars.

### 2.1. Turbulent Flow over Smooth Walls

Turbulent structures in wall bounded flows have been studied and reviewed extensively over the years by various researchers ((Fukagata, Iwamoto, & Kasagi, 2002; Jiménez & Pinelli, 1999; Marusic & Monty, 2019; McKeon, 2017), etc). Wall bounded turbulent flows are governed by the interaction of inertial and viscous forces (Smits & Marusic, 2013). The inertial-forces work to generate velocity fluctuations which are then damped by the action of viscous forces. This interaction is governed by different scales of turbulent structures depending on its distance from the wall (Jiménez, 2004). Viscous forces are significant in the near wall region while inertial forces dominate in the outer-region. As viscosity is an important parameter in the inner region, a viscous length and velocity scale is defined to characterize the turbulent flow close to the wall. The velocity scale is defined by the friction velocity  $u_\tau$  and the viscous length scale  $\delta_v$  as:

$$u_\tau = \sqrt{\frac{\tau_w}{\rho}} \quad (2.1)$$

$$\delta_v = \frac{\nu}{u_\tau} \quad (2.2)$$

Here  $\tau_w$  is the tangential wall shear stress,  $\rho$  is the fluid density and  $\nu$  is the kinematic viscosity. In the outer region of the flow, the boundary layer thickness  $\delta$  is used as the length scale. The outer streamline velocity  $U_\infty$  or the mean center line velocity  $U_c$  in pipe flows, is used as the outer velocity scale. Using the length scales, a non-dimensional

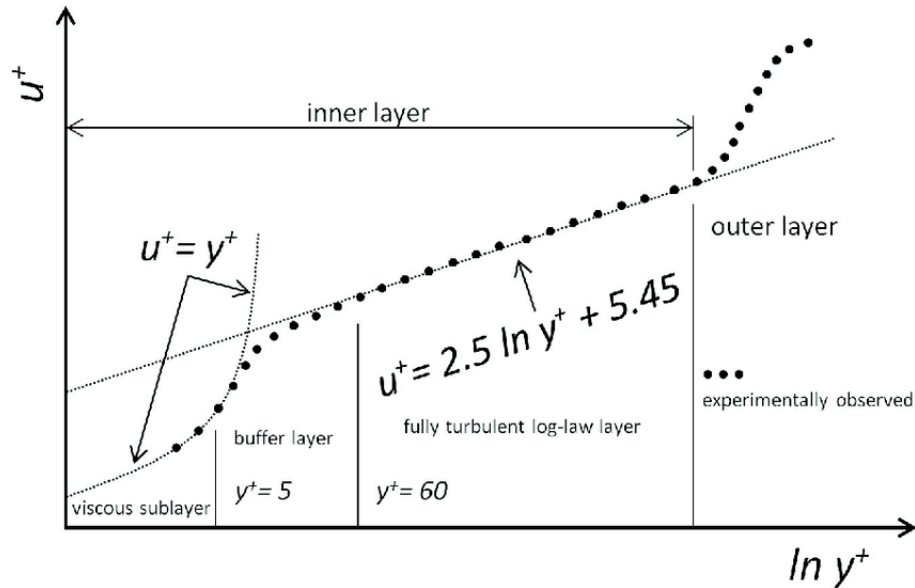


*Figure 2.1* Law of the wall: The velocity profile is defined for different regions in the flow. In the viscous sub-layer the flow is dominated by viscous scales only. In the log-layer, inertial scales are dominant. The buffer layer is where both inertial and viscous forces dominate (Mehta et al., 2018).

parameter is defined to characterize the flow. The friction Reynolds number, defined below, quantifies the relation between the outer length scale, ( $\delta$ ) and the viscous scale,  $\delta_v$ .

$$Re_\tau = \frac{u_\tau \delta}{\nu} = \frac{\delta}{\delta_v} \quad (2.3)$$

Figure 2.1 (Mehta et al., 2018) presents the law of the wall for turbulent flow over smooth walls. The different flow regions are differentiated based on the velocity profiles. Wall units,  $y^+$ , is the inner wall normal co-ordinate defined as  $y^+ = y/\delta_v$ . In the viscous sub layer,  $y^+ < 5$ , the flow is laminar and independent of the mean flow. The log layer is defined in the region  $y^+ > 60$ . In the log-region the velocity follows a log-profile and the flow is fully turbulent. The buffer layer,  $5 < y^+ < 60$ , is the layer between log and viscous sub layer. The formulation of the law of the wall is presented below:

$$U^+ = f_w(y^+) \quad (2.4)$$

The wall function  $f_w$  has been experimentally verified to be universal for canonical flows.

It can be determined based on  $y^+$ , i.e., the distance from wall in wall-units. In the viscous sub-layer this relation is expressed as:

$$U^+ = y^+ \quad (2.5)$$

In the log-law layer,

$$U^+ = \frac{1}{\kappa} y^+ + A \quad (2.6)$$

where  $\kappa$  is the Von Kármán constant and A is a constant to be determined experimentally.

### 2.1.1. Energy Cascade and Near-Wall Production Cycle

Wall bounded turbulent flows are multi-scale in nature and there is a continuous transfer of energy across different flow scales. This energy cascade is critical to the generation and dissipation cycles of turbulence structures in wall-bounded flows. Thus, its understanding is a significant step towards the aforementioned goals of optimization such as drag reduction. The transfer of energy can be from large scale to small scales or the other way round depending on the type of flow. But it is generally accepted that in a homogeneous flow, the energy is transferred from the largest scales to the the smallest scales also known as Kolmogorov scales (see Figure 2.2 (Makris et al., 2016)). This assumes that the size of the energetic eddies is considerably larger than the dissipative eddies. For most high Reynolds number flows, this is true away from the wall but breaks down in the near-wall region. Near the wall, a reverse cascade can exist as the eddy sizes are comparable across the energy spectrum (Smits & Marusic, 2013).

Kline et al. observed in 1967 that the near wall region was responsible for the significant production of turbulence in wall-bounded flows (Kline, Reynolds, Schraub, & Runstadler, 1967). Velocity streaks present in the near wall region slowly move away in an event described as streak ejection. This is followed by rapid oscillations of the streaks as they enter the overlap or buffer region ultimately resulting in breakdown known as the turbulent burst. Over the years many mechanisms have been proposed to explain this process of turbulent production. One such proposal suggests that the velocity streaks are

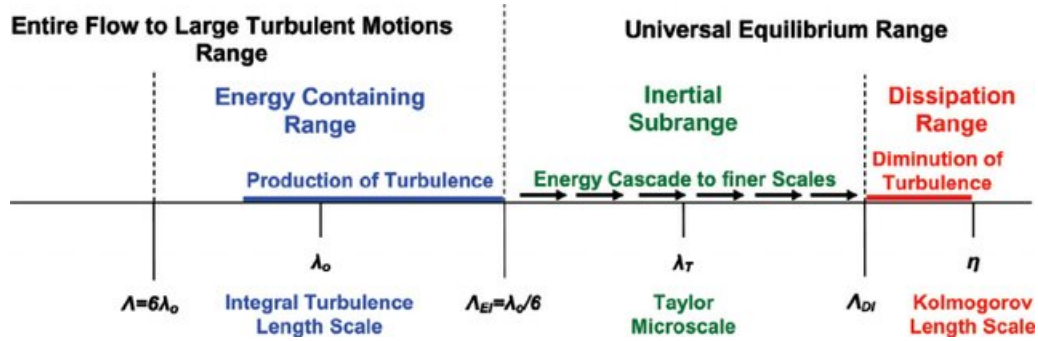


*Figure 2.2* The figure illustrates the energy cascade. Energy is transferred from the energetic containing scales to the dissipative scales (Makris et al., 2016).

generated by a pair of counter-rotating vortices (Blackwelder & Eckelmann, 1979; Swearingen & Blackwelder, 1987). The streaks are inherently unstable and break apart to produce tilted vortices. This has been described as the streak cycle (Jiménez & Pinelli, 1999). An alternate mechanism proposed by Smith, Walker, Haidari, and Sobrun (1991) suggests that stream wise vortices interact with the wall to induce a layer of vorticity in the opposite direction which is then stretched and strengthened under the action of mean shear. This interaction may lead to direct generation of velocity streaks. Both the mechanisms have been observed in nature but Jiménez and Pinelli's numerical investigations showed that the streak cycle was far more dominant than the wall cycle. This is an important conclusion from this study as will be seen in a subsequent section where the impact of surface roughness on wall bounded turbulence is discussed.

## 2.2. Turbulent Flow over Rough Walls

Turbulent flow over rough surfaces depends on the nature of the roughness. A review of the literature on the effect of roughness on turbulence reveals that there are two important non-dimensional parameters used to define the nature of roughness. The roughness Reynolds number  $k_s^+$ , is defined as:

$$k_s^+ = \frac{k_s u_\tau}{\nu} \quad (2.7)$$

where  $k_s$  is the equivalent roughness height,  $u_\tau$  is the friction velocity and  $\nu$  is the kinematic viscosity of the fluid. The roughness Reynolds number is used to characterize the roughness of the surface. A surface with  $k_s^+ < 5$  is defined as a hydraulically smooth surface. Transitionally rough surfaces are those with  $5 < k_s^+ < 60$  while roughness with  $k_s^+ > 60$  is referred to as fully developed roughness.

Nikuradse and Nikuradse (1933) was one of the first to describe a velocity profile for rough surfaces. They experimentally identified that the log law profile could still be observed for flow over rough surfaces. For a surface roughness that follows a power law,  $k_s = Kx^n$ , where  $x$  is the streamwise coordinate of the location in study and  $k_s$  is the local equivalent roughness height, this relation can be defined as follows:

$$U^+ = \frac{1}{\kappa} \left[ \log\left(\frac{(z + \varepsilon)u_\tau}{\nu}\right) + \Pi W\left(\frac{z}{\delta}\right) \right] - \Delta U^+(k_s^+) + A \quad (2.8)$$

where  $\kappa$  is the von Kármán constant,  $A$  is a constant offset,  $W$  the wake function,  $\Pi$  is the Coles wake factor,  $\varepsilon$  is the roughness offset and  $\Delta U^+$  is the roughness function. The roughness function is used to quantify the effect of roughness on mean velocity profile (Sridhar, Pullin, & Cheng, 2017). Different forms of the roughness function have been proposed by various studies. One such form was presented by Sridhar et al. (2017) for fully rough flow.

$$\Delta U^+(k_s^+) = \frac{1}{\kappa} \log(k_s^+) + A - B \quad (2.9)$$

The focus of this review has so far been on k-type rigid roughness elements. Roughness can be classified two different types of roughness based on the geometry of the roughness: k-type and d-type (see Figure 2.3). In 1969, A. Perry, Schofield, and Joubert (1969) conducted an experiment to differentiate between k-type and d-type roughness. The study confirmed that for k-type roughness, equivalent roughness  $k_s$  depends on the size of the roughness. On the other hand, the roughness function for d-type roughness doesn't depend on the size of the roughness but rather depends on an outer scaling length like the diameter of the pipe. Perry et al. proposed the following expression for roughness

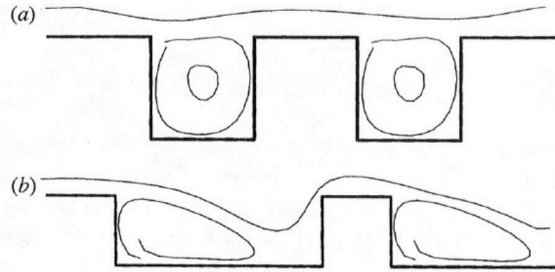


*Figure 2.3* a. d-type grooves in the surface. It has been hypothesized that the deep grooves sustain stable re-circulation vortices that isolate the roughness from the mean flow. b. k-type grooves in the surface have a width greater than 3-4  $k$  which results in a re-circulation bubble that reattaches ahead of the next groove exposing the roughness to the mean flow (Jiménez, 2004).

function of d-type roughness:

$$\Delta U^+ = \frac{1}{\kappa} \log\left(\frac{du_\tau}{2\nu}\right) + A - \frac{3}{2\kappa} - \eta - \frac{U_b}{u_\tau} \quad (2.10)$$

where  $U_b$  is the mean bulk velocity and  $A$  and  $\eta$  are constants. The expression clearly illustrates the dependence of the roughness function on the outer scaling length 'd', the pipe diameter, instead of the roughness size 'k'.

### 2.2.1. Effect of Roughness on The Mean Flow

The classical view with regards to the effect of roughness on the mean flow and the turbulence structures in the mean flow states that this effect is mostly insignificant. A. E. Perry and Abell (1977) confirmed the Townsend's hypothesis (Townsend, 1956) which states that all the mean relative motions and energy containing components of the turbulent flow are independent of viscosity and surface friction. No significant difference was observed in the energy spectra for flow over rough and smooth surfaces in the outer region of the flow ( $y/R > 0.15$ )(see Figure 2.4.). A nylon mesh with a hexagonal weave and a nominal height of 0.25 mm was used as the roughness. Sabot et al. (1977) studied a very rough pipe with ring like slats with a  $3 \times 3$  mm square cross-section. The study concluded that the presence of roughness did not fundamentally alter the turbulence production cycle as observed over a smooth wall and the same mechanisms were at work

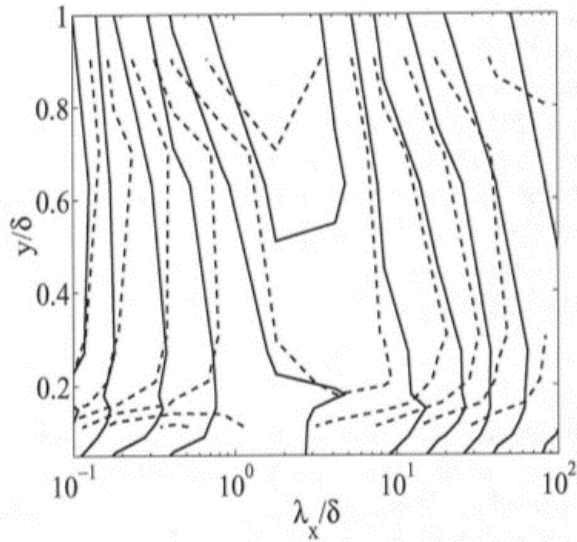


*Figure 2.4* The figure shows Pre-multiplied spectral density  $k_x E_{uu}$ , as a function of the stream-wise wavelength  $\lambda_x = 2\pi/k_x$ , and of the wall distance —, smooth wall, - - - , rough wall (Jiménez, 2004).

over a rough wall too. No significant change in the integral length scales was observed when compared with the smooth wall. However, a study of the turbulence intensity profiles noted an increase in the anisotropy of turbulence which the authors suggested was an indication of possible influence of the rough surface on the coherent structures in the near wall region. Figure 2.5 shows the integral length scales of the velocity components as a function of the distance from wall.  $L_{11}$ , represented on the plot as an unfilled square, is the integral length scale of the streamwise velocity component in the streamwise direction while  $L_{22}$ , represented on the graph as a filled square, is the the integral length scale of the radial velocity component in the streamwise direction. A slight shift away from the wall of the maximum value of  $L_{11}$  is observed for the rough wall.

Nakagawa and Hanratty (2001) conducted PIV experiments of flow over a sinusoidal wall with a length of 5mm and amplitude of 0.25 mm. Similarity was observed in the turbulent stresses. The study concluded that the measurements proved the universality of turbulence and turbulent structures irrespective of the surface characteristics. Krogstad, Antonia, and Browne (1992) was the first to seriously challenge the classical view espoused by the research reviewed so far. Measurements were taken in a zero-pressure

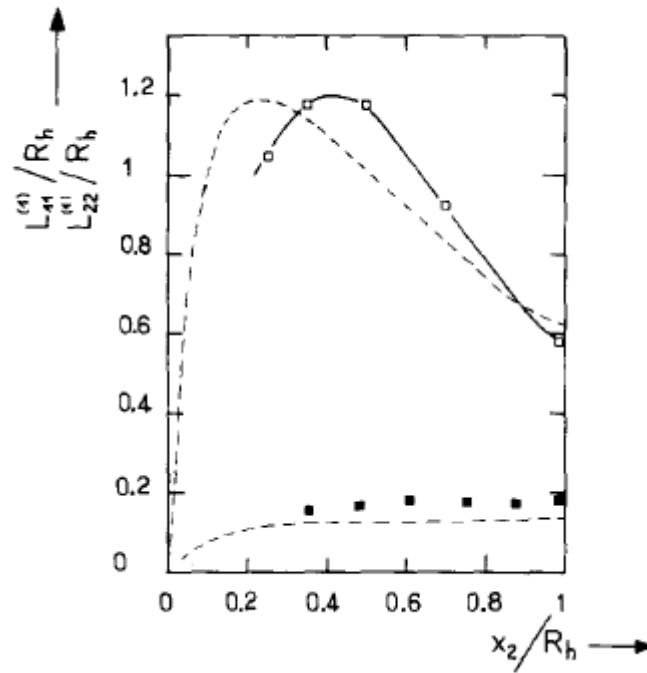


*Figure 2.5* Integral length scales of the velocity components as a function of distance from the wall. The filled square is the integral length scale of the radial velocity component in the streamwise direction ( $L_{22}$ ). The unfilled square is the integral length scale of the streamwise velocity component in the streamwise direction ( $L_{11}$ ). —, rough pipe, - - - , smooth pipe (Sabot et al., 1977).

gradient turbulent boundary layer over a mesh screen roughness. The mesh was made with 0.69 mm wires with a center-line spacing of 3.18 mm. The authors noted that the surface roughness influenced the mean velocity and turbulence intensity profile even in the outer region. It was also observed that the one-point correlation-times below  $y/\delta < 0.5$  for rough wall were about twice shorter compared with the smooth wall.

More recently, a study by Monty et al. (2010) observed a reduction in energy contribution of the large scale eddies due to the introduction of braille type roughness elements with a height of about 400 microns (Figure 2.6). The study also observed an increase in the amplitude modulation coefficient in the near wall region. Amplitude modulation coefficient ( $R_{AM}$ ) is used to characterize the interaction between large scale



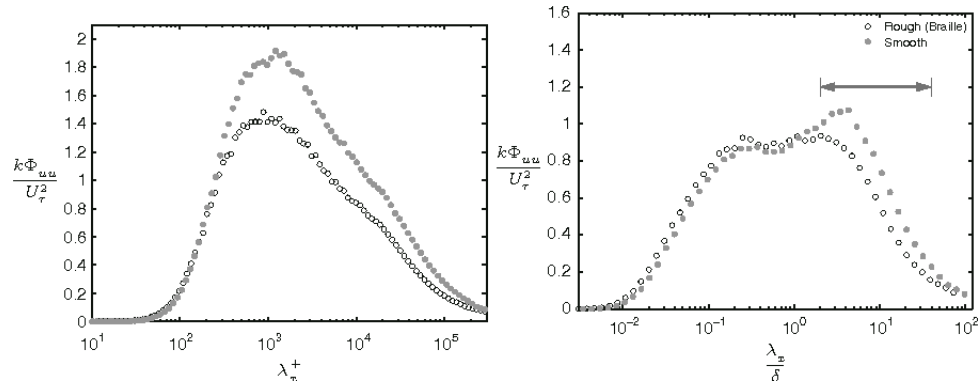


Figure 2.6 Pre-multiplied energy spectra for rough and smooth cases (Monty et al., 2010).

and small scale structures. It is defined as follows:

$$R_{AM} = \frac{u_L E_L(u_s)}{(\sqrt{\bar{u}_L^2}) \sqrt{E_L(u_s^2)}} \quad (2.11)$$

Here,  $u_L$  is the large-scale component of the streamwise velocity fluctuations and  $E_L(u_s)$  is the filtered large-scale envelope of the streamwise small-scale fluctuations. The observations of Monty et al. (2010) further highlighted that the impact of roughness extended beyond the near wall region. Using a predictive model, Inner-Outer Interaction Model (IOIM), Squire, Baars, Hutchins, and Marusic (2016) made several important predictions regarding the interactions between the inner and outer regions of the flow over rough surfaces. The linear interaction between the inner and outer large scale energy content reduced for rough surfaces when compared with smooth surfaces. Interestingly, the shape and extent of these interactions were similar for both smooth and rough walls but the energy of these large scale events was reduced for rough surfaces. Along with the reduced interaction of the large scale structures, the study also concluded that there was an increase in the modulation of the small scales in the inner region for flow over rough walls.

The studies reviewed thus far show that directed and patterned roughness may have potential benefits. Shark skin inspired riblets are an example of attempts to use directed roughness patterns for drag reduction applications (see Figure 2.7). Vishwanath (2002) reviewed experimental research on drag-reduction on 2-D aerofoils via riblets. The review

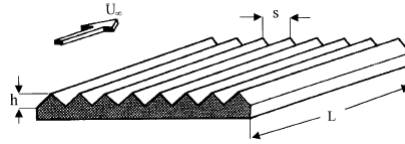


*Figure 2.7* Example sketch of riblet geometry. The riblet film had a height of 0.114 mm and was studied under both sub-sonic and supersonic conditions (Vishwanath, 2002).

concluded that the riblets led to a 5-8% drag reduction depending on the flight regime. The measurements were made for riblet films with  $h = 0.114\text{mm}$  for both subsonic and supersonic flight regimes. The reduction in drag was attributed to the suppression of the ejection events in the near wall region which led to a reduction in the turbulence intensity for the flow over riblets. The study also concluded that the application of the riblets would be more useful in an adverse pressure system. Under adverse-pressure conditions, the riblets lead to the thickening of the viscous sub-layer, reduced turbulence intensity and Reynolds stresses. They also reduced turbulent production by inhibiting the velocity streak ejection cycle near the wall.

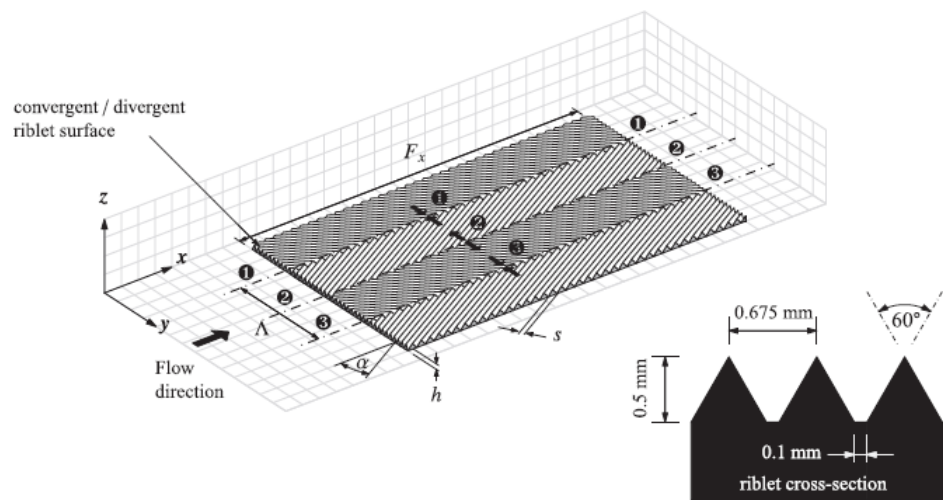


*Figure 2.8* Sketch of converging-diverging riblet geometry used by Nugroho et al. (2013). The height of the riblets was 0.5 mm and the spacing was 0.675 mm (Nugroho et al., 2013).

Nugroho et al. (2013) studied the herringbone type riblets in a zero-pressure gradient boundary layer. Herringbone here refers to the arrangement of riblets i.e., the riblets were

arranged in a converging-diverging pattern (see Figure 2.8). The height of riblets used was 0.5 mm and the spacing between them was 0.675 mm. The converging-diverging sections of the riblets imposed a span-wise periodicity onto the turbulent boundary layer modifying the mean flow along the span-wise direction. The local mean velocity increased over the diverging sections which led to a decrease in the turbulence intensity and a thinner boundary layer. Conversely, the local mean velocity decreased over the convergent sections which lead to an increase in the turbulence intensity and a thicker boundary layer. The secondary structures generated due to the riblets were observed to decrease the large scale energy over the diverging section while the opposite was true over the converging sections. Chen et al. (2014) also studied the herringbone riblets for drag reduction applications. The study designed novel herringbone riblets inspired from the feather arrangement on mature pigeons (shown in Figure 2.9). These nature inspired designs led to an 17-21% decrease in the drag, a higher reduction when compared with conventional riblets.

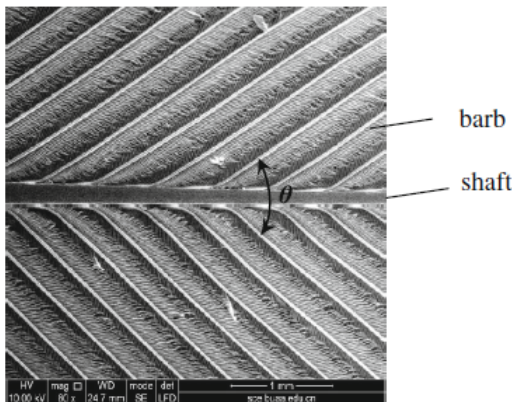


*Figure 2.9* Microscopic features of bird flight feathers used by Chen et al. (2014) to design bio-inspired herringbone riblets. The bio-inspired riblets reduced the drag by about 17-21% (Chen et al., 2014).

To summarize, while most earlier work agreed that the impact of roughness on the flow is limited to the near wall region, recent studies have shown that the effect of roughness may extend beyond the near wall region. For example, Monty et al. (2010) showed the potential for affecting large scale structures in the outer region, also referred to

as "superstructures", by using small roughness elements on the wall surface. Riblets have also shown potential for drag reduction with Vishwanath (2002) review of the relevant showing a 5-8% decrease in drag. Unconventional riblets like the herringbone riblets have yielded even better results with Chen et al. (2014) designing bio-inspired herringbone riblets that reduced the drag by 17 -21%. But, the focus of research in this area has been predominantly on the impact of rigid roughness elements on the flow. Recently though, there has been rising interest in flexible roughness elements and their effect on the flow.

### 2.3. Turbulent Flow over Flexible Roughness Elements

Toloui et al. (2019) conducted a study to observe the difference between dynamic and rigid roughness elements. Experiments were conducted with a set of tapered flexible/rigid cylinders with base diameter  $d = 0.55\text{mm}$ , height  $k = 3\text{mm}$  and a spacing  $\lambda = 4\text{mm}$  between the cylinders. Digital inline holographic particle tracking velocimetry (DIH-PTV) was used for simultaneous measurements of the 3D turbulent flow. The rigid and flexible roughness were studied under the same flow conditions:  $Re_h = 32500$  based on the center-line velocity  $U_c = 0.65\text{m/s}$  and channel width  $h = 2\delta = 50\text{mm}$ .

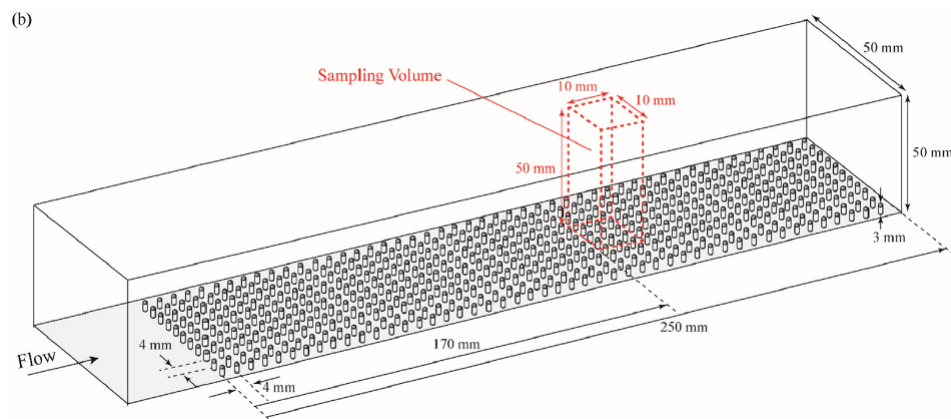


Figure 2.10 Schematic of the experimental setup (Toloui et al., 2019).

Toloui et al. (2019) observed a significant decrease in the Reynolds stresses for flexible roughness when compared with the rigid roughness elements (Figure 2.11). The compliance of flexible roughness elements was observed to dampen the turbulence close to the wall ( $y < 2k$ ). Flexible roughness elements also led to a decrease in the total kinetic

energy (TKE) of the flow (see Figure 2.12). The authors compared the deficit in TKE and the increase in the strain energy of the roughness elements and hypothesized that the kinetic energy of the flow was being converted into strain energy.

Jacobi and McKeon (2011) investigated a dynamic roughness in a turbulent boundary layer. The experiment was conducted in a zero-pressure gradient boundary layer wind tunnel. The roughness consisted of four spanwise k-type roughness bars with a thickness of 1.57mm (see Figure 2.13). The root-mean-square height of the motion of the roughness was 1.16 mm. An organized wave was introduced in the flow due to the wave like behavior of the roughness impulse. This wave was observed to persist as far as  $20\delta$  downstream of the roughness. This illustrated the ability of small dynamic roughness elements to affect the turbulent boundary layer.

Winzen, Klaas, and Schröder (2013) studied the influence of hairy surfaces on the flow over a wing. The hairy surfaces used for the study were inspired by the velvet like hairy surface of a barn owl wing. The flow re-attached earlier for hairy surfaces when compared with a clean surface. The redistribution of turbulent kinetic energy forced the flow to transition earlier than a smooth surface enabling it to reattach faster. The hairy surfaces also led to the reduction of the separation bubble on the suction side of the wings. Thus the study observed an increase in the aerodynamic efficiency of the wing due to the presence of the hairy surfaces.

Brücker (2011) investigated the interaction of near-wall turbulence with hairy surfaces

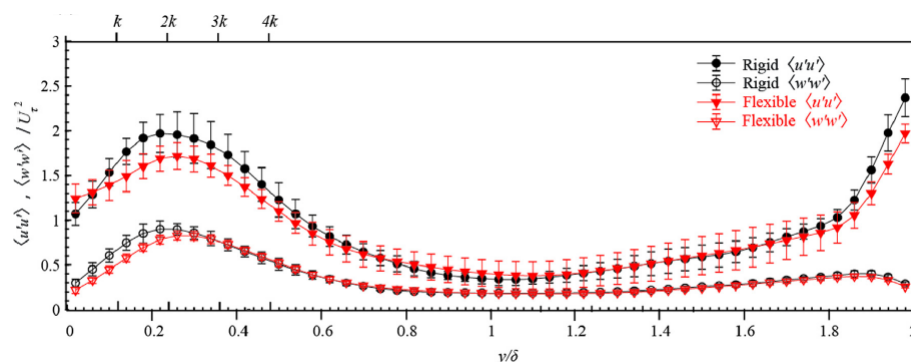


Figure 2.11 Reynolds stresses for rigid and flexible roughness elements (Toloui et al., 2019).

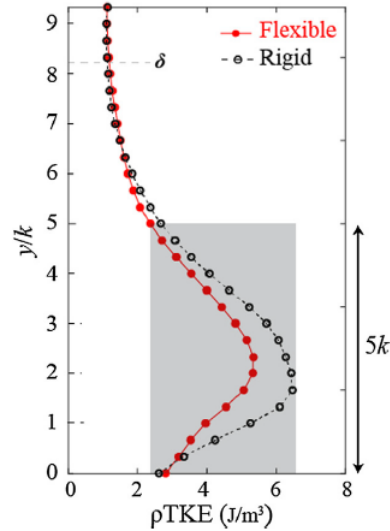


Figure 2.12 Total Kinetic Energy for rigid and flexible roughness elements (Toloui et al., 2019).

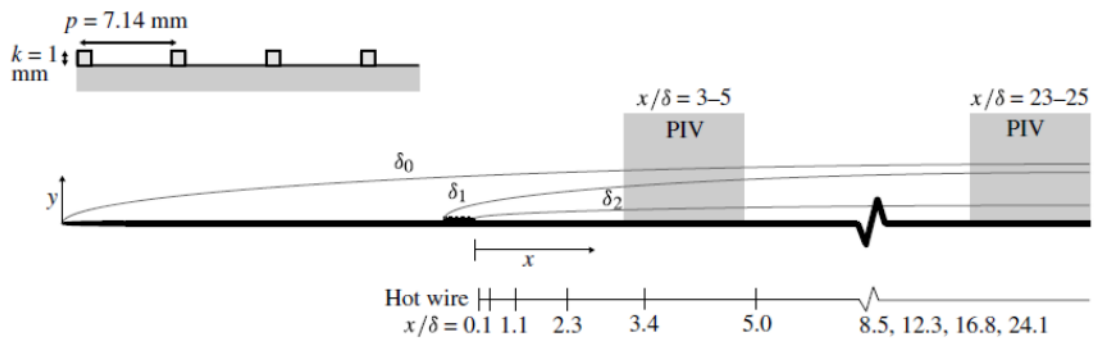
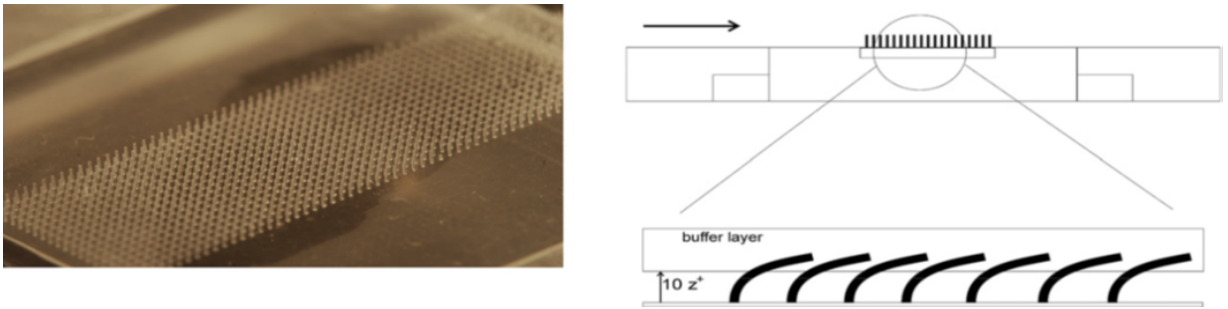


Figure 2.13 The figure shows the four k-type roughness bars used as dynamic roughness by Jacobi and McKeon (2011). Different hot wire measurement locations are also shown (Jacobi & McKeon, 2011).

in a turbulent boundary layer flow along a flat plate in an oil channel at  $Re = 1.2 \times 10^6$ . The hairy carpet used for the experiment consisted of micro-hairs with a height of 1 mm arranged in an array of  $60 \times 30$ . The array spacing was  $500\mu\text{m}$  in streamwise direction and  $1000\mu\text{m}$  in the spanwise direction. The presence of micro-pillars was shown to have a spanwise anisotropic damping effect. The micro-pillars also promoted varicose waves and inhibited sinusoidal waves in the flow. This led to an increase in coherence lengths in both the streamwise and spanwise direction. Based on these observations, the author assumed that the presence of micro-pillars suppressed the formation of velocity streaks. Near wall



*Figure 2.14* The figure illustrates a dense carpet of elastomeric micro-hairs of length 1mm arranged in a regular grid (60 by 30) (Brücker, 2011).

streak stabilization has been shown to be an indicator of drag reduction. Thus, the suppression of velocity streaks indicates that micro-pillars may lead to a reduction in turbulent drag.

The role of engineered rough surfaces towards the goal of optimization has evolved over the years. Use of riblets for drag reduction represents the most prominent of such applications. Use of patterned roughness elements to reduce drag is the next step in this evolution. The observation that the effect of the roughness elements extended into the outer layer is crucial to the development of engineered rough surfaces for the purposes of drag reduction. Recently, patterned flexible roughness have exhibited a potential for engineering benefit. The current work focuses on investigating that potential through the use of HAMuP arrays. The next chapter outlines the manufacturing process for HAMuP arrays and the experimental set-up used to investigate their effects.

### 3. Description of the Experiment

This chapter presents the details of the experimental setup. First, the HAMuP manufacturing setup is presented. This is followed by a description of the experimental setup used to carry-out hot-wire measurements.

#### 3.1. HAMuP Manufacturing Setup

The manufacture of High-Aspect Ratio Micro-pillars (HAMuP) is a two-part process: (i) manufacturing of the wax mold followed by (ii) casting of micro-pillars under vacuum. The wax mold is manufactured by punching a set of holes in a wax sheet using a micro-needle. Silicone rubber is then poured on the wax mold under vacuum and cured for 24 hours to obtain a HAMuP array. The following sections further elaborate on the manufacturing process.

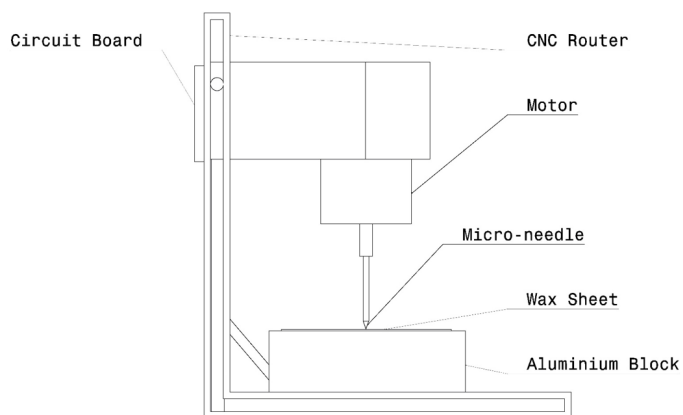
##### 3.1.1. Manufacturing the Micro-pillar Mold

Figure 3.1 shows the schematic of the LinkSprite DIY CNC 3 axis 2418 Engraver machine used to punch holes in a wax sheet. Two stepper motors are used for movement in the  $x - y$  plane. A spindle motor is used to spin the needle if required. An arduino circuit board in combination with a Grbl controller is used to control the machine. Grbl is an open source, high performance software that is used to control the motion of CNC machines (*GRBL:About*, 2017). Grbl accepts standard G-code instructions.

The first step of the manufacturing process is to mill the surface of the wax using a milling tool. This ensured that the wax surface was uniform and was also normal to the drill chuck. The G-code file, with instructions for manufacturing the mold with a  $55 \times 120$  array of micro-holes, was generated using a Matlab code. The spacing was set as 1mm in span-wise direction and 0.5 mm in the stream-wise direction.

Certain precautions were taken to ensure consistency in the micro-pillar mold quality. Every hole was punched twice to ensure the hole was clear of wax. The G-codes also directed the CNC router to punch the holes in steps instead of plunging the needle into the wax sheet all at once. This was important to ensure a longer life for the micro-needle and to avoid breakage.





*Figure 3.1* Schematic of the CNC router used to punch holes in the wax sheet to create the micro-pillar molds

### 3.1.2. Casting the HAMuP Array

The silicone rubber is poured into the mold inside an unbreakable, transparent poly-carbonate vacuum chamber. Two magnets, one on the inside and one on the outside, are used to pour the silicone rubber in a controlled fashion (see Figure 3.2). The vacuum chamber is connected to vacuum pumps to ensure vacuum of 29 in-Hg in the chamber. This is necessary to purge the air-bubbles trapped in the holes.

Smooth-on solaris elastomer was the material used to make the micro-pillars. The Smooth-On solaris silicone rubber comes in two parts, A and B, which are mixed in 1:1 ratio to manufacture the silicone rubber. This process results in trapped air-bubbles in the silicone rubber mix. To remove these air bubbles, the mix is placed in vacuum. This brings the air-bubbles trapped in the mix to the surface. To get rid of these air bubbles, the vacuum pipe is disconnected abruptly to expose the surface air bubbles to atmospheric pressure. This process is referred to as "shocking" for the purposes of this study. Care is taken to disconnect the chamber from the vacuum pump to avoid damaging it during this process.

After repeated shocking to remove the air-bubbles, the silicone rubber is poured on to the mold under vacuum. The silicone rubber is poured in layers. After every pour, the



*Figure 3.2* The vacuum chamber apparatus used for casting of micro-pillar arrays.

entire system is shocked to break any air-bubbles still trapped in the pour. An aluminum block is used to hold the silicone rubber pour as it enters the holes. The excess silicone rubber poured acts as a base for the micro-pillar array. After filling the aluminum block to the top, the silicone rubber is left to cure for 24-48 hours. The longer the curing time, the easier it is to extract the pillars from the mold. A close-up view of the micro-pillars array manufactured using this process is shown in Figure 3.3.

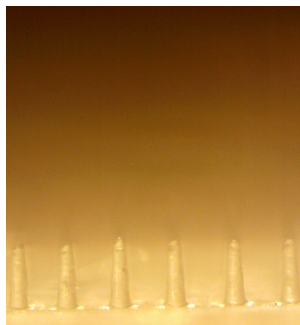


*Figure 3.3* A small section of the HAMuP array showing individual micro-pillars.

### **3.1.3. HAMuP Array**

Three micro-pillar sets were manufactured with varying parameters for this thesis. Their key properties are summarized in the table below:

Array 1 and 2 differ only in the resin-hardener ratio. Array 2 was prepared with 80% hardener to create a softer array. Array 3 micro-pillars are taller with a smaller diameter. Hot-wire measurements were carried out at three different locations over the HAMuP array. These locations are shown in Figure 3.4.

Table 3.1

Table of parameters for different HAMuP arrays manufactured

Parameter	Array 1	Array 2	Array 3
Array Size	55 × 120	55 × 120	55 × 120
Spacing (spanwise × streamwise)(mm)	1 × 0.5	1 × 0.5	1 × 0.5
Pillar Height(mm)	0.6	0.6	0.735
Pillar Average Diameter(mm)	0.135	0.135	0.1
Resin-Hardener Ratio	1 : 1	1 : 0.8	1 : 1

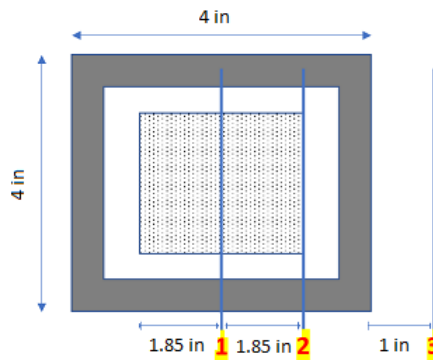
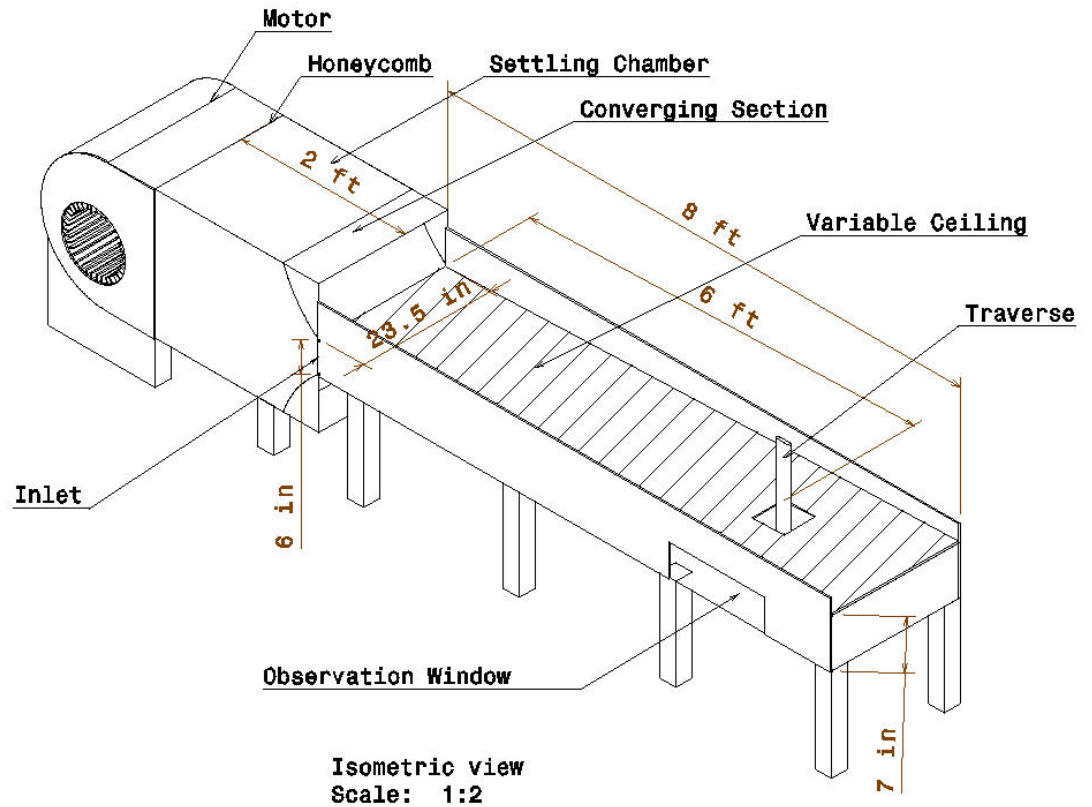


Figure 3.4 Hot-wire measurement stations over the HAMuP array

### 3.2. Hot-wire Anemometry

All the velocity measurements were made using a 5  $\mu\text{m}$  hot-wire with an aspect ratio of about 200. The technique used to carry-out these hot-wire measurements is known as Constant Temperature Anemometry(CTA). CTA is based on the cooling effect of a flow on a heated body, in this case the hot-wire which is maintained at a constant temperature. An in-house anemometer was used to measure the voltage readings corresponding to the flow velocity at an overheat ratio of 1.8. The hot-wire voltage was acquired using a data acquisition board DT-9836 which was controlled through MATLAB scripts on a connected computer. The DT-9836 is a 16 bit analog/digital system with an input voltage range of  $\pm 10\text{V}$ . An OMEGA differential pressure transmitter was used to measure the dynamic pressure and subsequently the free-stream velocity. A National Instruments thermocouple was used to measure the fluid temperature.



*Figure 3.5* Experimental facility 1: zero-pressure gradient wind tunnel. The measurements were carried out 6 ft from the sandpaper trip at the inlet.

The experimental data was collected in two different facilities. The data for location 1 for all the three HAMuP arrays was collected in a zero-pressure gradient wind-tunnel with a variable height ceiling (Experimental Set-up 1, see Figure 3.5). The data at location 2 and 3 was collected for HAMuP arrays 1 and 3 in a larger wind-tunnel (Experimental Set-up 2, see Figure 3.6).

For experimental set-up 1, the test section  $6 \times 23.5$  inches wide and the HAMuP array was placed 6ft from the inlet. It was placed in a cavity in the floor of the tunnel. Variable height ceiling is used to maintain a zero-pressure gradient in the tunnel (see Figure 3.6). The boundary layer is tripped using a strip of sandpaper at the inlet.

Experimental set-up 2 is a 25 ft long boundary layer wind-tunnel (see Figure 3.7). The

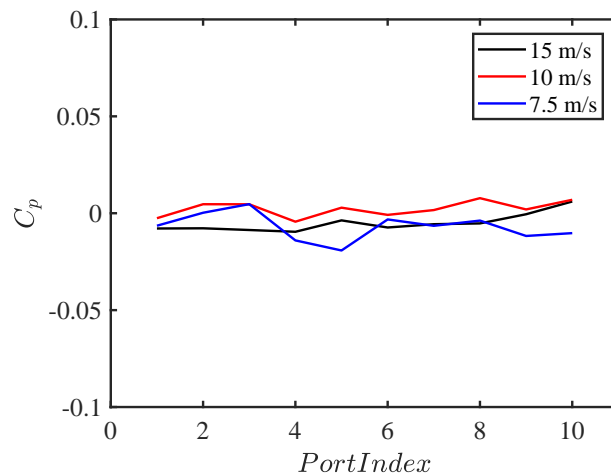


Figure 3.6  $C_p$  v  $x$  for the zero-pressure gradient wind tunnel measured at three different velocities. The  $\Delta C_p$  was less than 0.01 for all the different velocities. Each port was separated by a distance of 6 inches.

HAMuP array was placed about 20 ft from the inlet. A sandpaper trip was used to trip the boundary layer at the inlet of the tunnel.

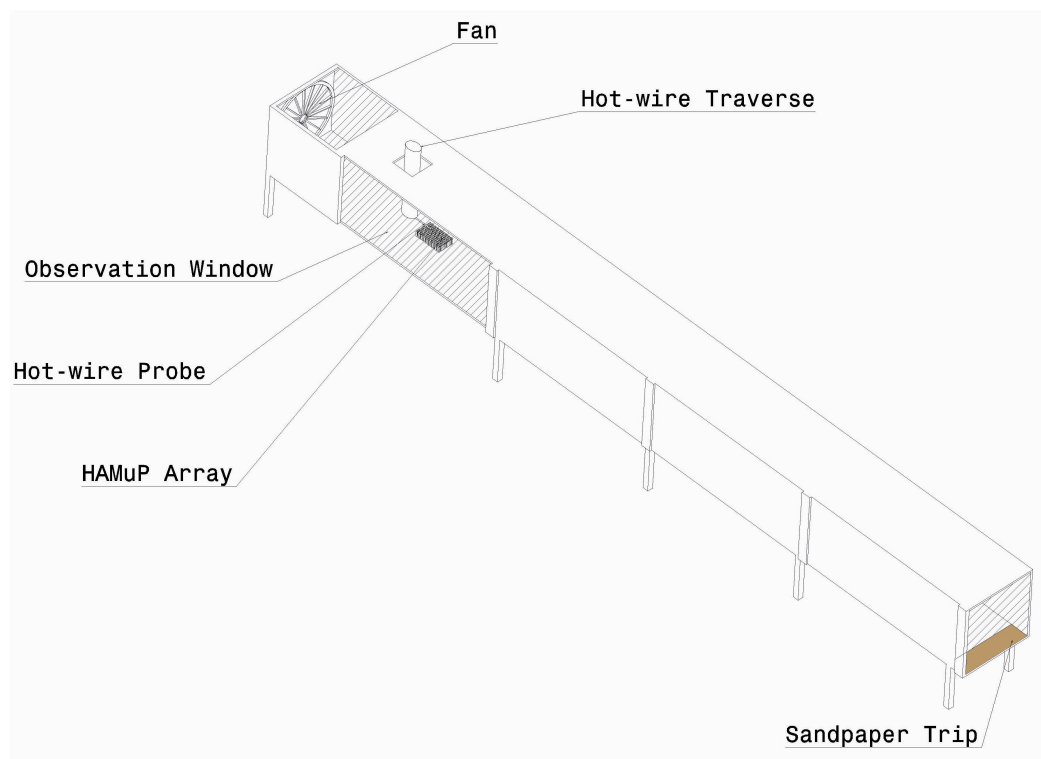
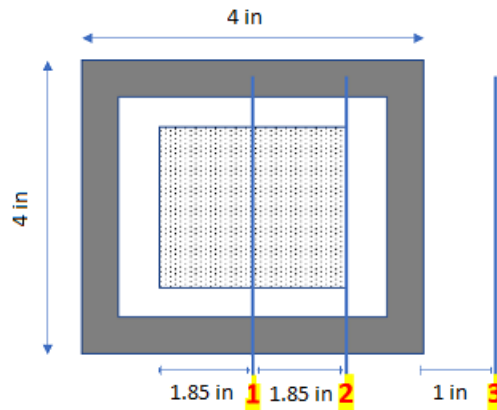


Figure 3.7 Experimental Set-up 2: 25 ft long Boundary Layer Wind Tunnel.

## 4. Results and Discussion

Hot-wire measurements were conducted to obtain the wall normal velocity distribution over a HAMuP array. The measurements were conducted at three different stream-wise locations as described in the previous chapter(see Figure 4.1). A parametric approach was adopted to further study the effect of HAMuP arrays on turbulent boundary layer. HAMuP array 2 was manufactured to be softer (lower  $E_p$ ) to investigate the effects of elasticity and stiffness of the micro-pillars on the flow. The effect of height and diameter on the flow was studied using HAMuP array 3. HAMuP array 3 was manufactured with an average height of  $735\mu\text{m}$  and average diameter of  $100\mu\text{m}$ . All the flow measurements presented here are normalized with respect to the outer scales. The mean free-stream velocity,  $U_\infty = 14.5 \pm 0.2$  m/s, was maintained to be constant for all cases. The preliminary results for



*Figure 4.1* Hot-wire measurement locations for data collection

HAMuP array 1 are presented first. Important flow parameters like velocity, turbulent intensity, amplitude modulation coefficient, etc., were studied to get a preliminary picture of the flow physics over the HAMuP array.

### 4.1. Interaction of HAMuP Array with Wall Turbulence

Measurements over Location 1 (see Figure 4.1) are presented first. Figure 4.2 shows the mean velocity profile for the flow over HAMuP array 1 in comparison to the flow over a smooth surface at location 1. In the near wall region, a marked decrease in the mean velocity is observed for the case of HAMuP array when compared with a smooth

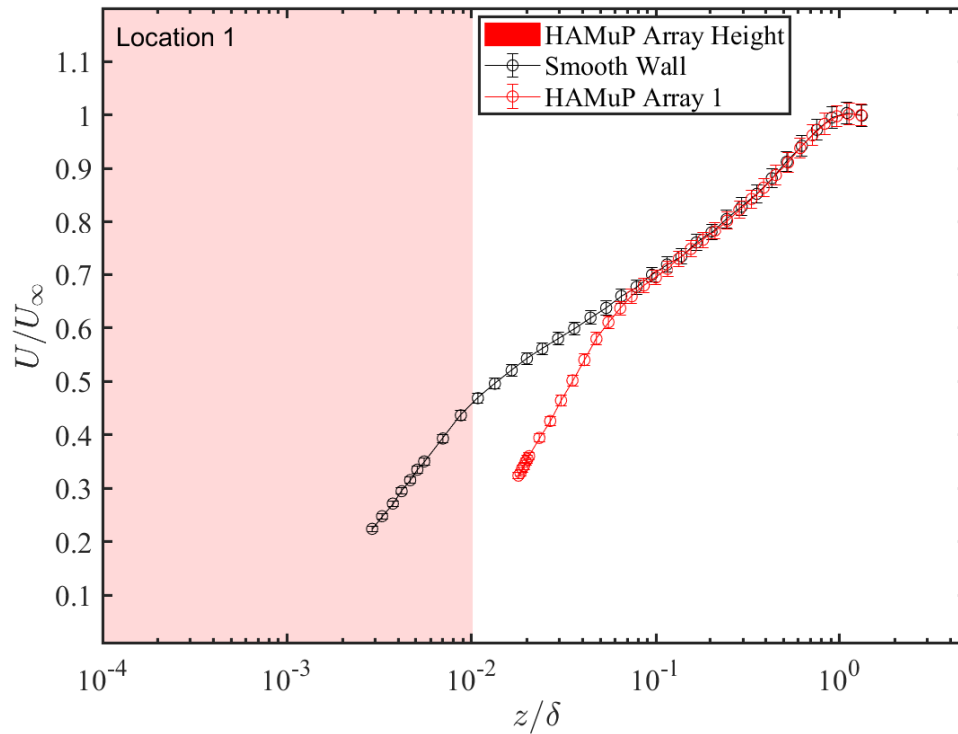


*Figure 4.2* The mean velocity profile  $U$  for HAMuP array 1 in comparison with the velocity profile over a smooth wall. The red region represents the approximate height of the HAMuP array.

surface. For example, at the wall normal location  $\frac{z}{\delta} = 3 \times 10^{-2}$  there is a 17% decrease in the normalized velocity for flow over HAMuP array 1. When compared with the smooth wall flow, the mean velocity profile for HAMuP 1 and smooth flow collapse on each other. The turbulence intensity profiles,  $\bar{u}^2/U_\infty^2$ , for the two flows are shown in figure 4.3. There is a shift in the inner turbulence intensity peak for the flow over HAMuP array when compared with a smooth wall. There is also a slight reduction in the peak in the case of the HAMuP array. However, the turbulence intensity profiles provide no information regarding the distribution of scales in the flow and their contribution to this turbulent activity. Thus, the turbulence intensity profile has been decomposed into its large scale and small scale components. The shift in the turbulence intensity profile is reflected in the shift of the small scale peak for the HAMuP array. The slight reduction of the turbulent intensity peak is due primarily to the reduction in the large scale intensity around the near wall peak.

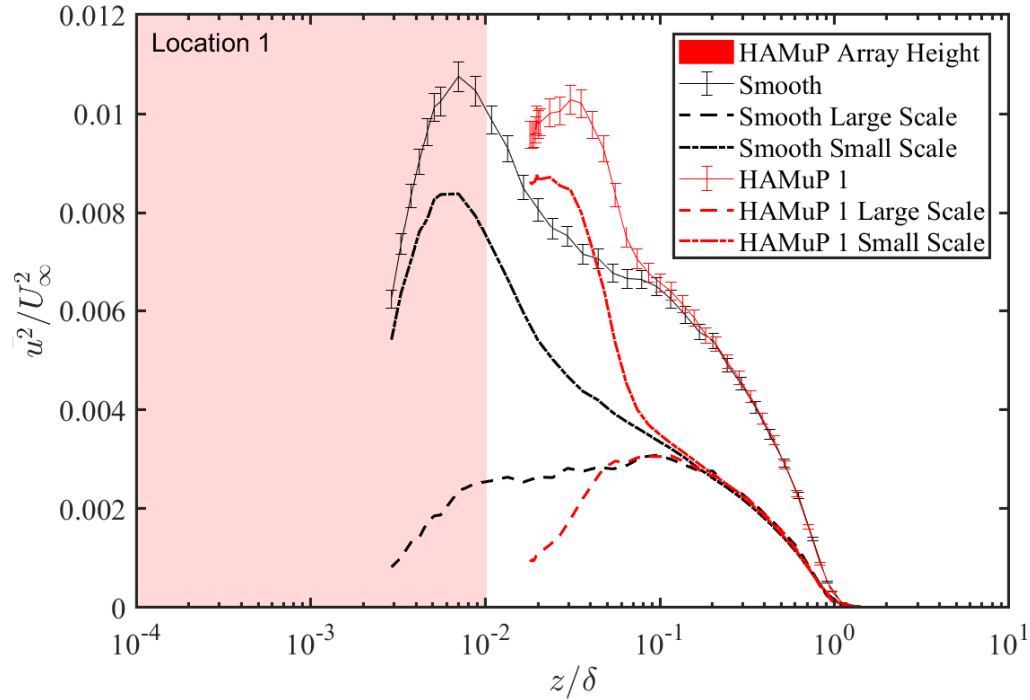


*Figure 4.3* The figure illustrates the turbulent intensity profiles for HAMuP array 1 in comparison with a smooth wall. Turbulence intensity for large and small scales in the flow is also shown. The red region represents the approximate height of the HAMuP array.

To further understand these changes, the energy spectra is considered. Figure 4.4 shows the outer normalized, pre-multiplied, 1-d streamwise energy spectra for flows over HAMuP 1 in comparison with the smooth wall. The dotted line divides the small and large scales in the flow. The red region represents the height of the HAMuP array.

Taylor's frozen turbulence hypothesis was used to convert the temporal data (frequency) to spatial data(wave-number) for the energy spectra. As seen in the turbulent intensity profiles, there is an observable increase in the energy of the small scale structures for flow over HAMuP array. The distribution of the most energetic structures is skewed towards smaller scales in the case of HAMuP array when compared with the smooth wall. There is an upward shift of the energetic scales away from the wall for HAMuP array.

Amplitude modulation co-efficient ( $R_{AM}$ ) characterizes the interaction between large-scale and small-scale structures. As discussed earlier, an amplitude coefficient  $R_{AM}$



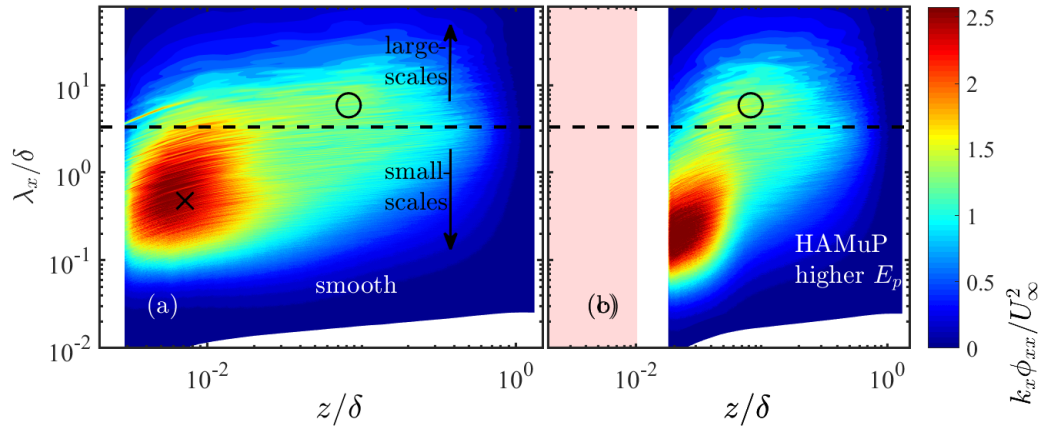


Figure 4.4 The figure here presents the outer normalized, pre-multiplied, 1-d streamwise energy spectra,  $k_x \phi_{xx}$ , for smooth wall and the HAMuP 1. The dotted line is the division between large scale and small scales. The red region represents the average height of the HAMuP array.

is defined as:

$$R_{AM} = \frac{u_L E_L(u_s)}{(\sqrt{\bar{u}_L^2}) \sqrt{E_L(u_s^2)}} \quad (4.1)$$

Here,  $u_L$  is the large-scale component of the streamwise velocity fluctuations and  $E_L(u_s)$  is the filtered large-scale envelope of the streamwise small-scale fluctuations. Figure 4.5 shows the  $R_{AM}$  for flow over smooth walls and HAMuP 1. In the near wall region, there is a significant increase in the amplitude modulation coefficient for the HAMuP array when compared with a smooth wall. When compared with the smooth wall, in the outer region, the amplitude modulation profiles both HAMuP array and smooth wall collapse on each other.

As discussed in earlier chapters, micro-pillars have been observed to serve sensory roles in nature (Tao & Yu, 2012). Line sensors in fishes serve to detect disturbances in flow created by incoming predators. The increased amplitude modulation observed for HAMuP arrays points to a possible mechanism by which the naturally occurring micro-pillars detect large-scale structures of the flow.

To summarize, there is a shift in velocity profile and the turbulent intensity peaks for

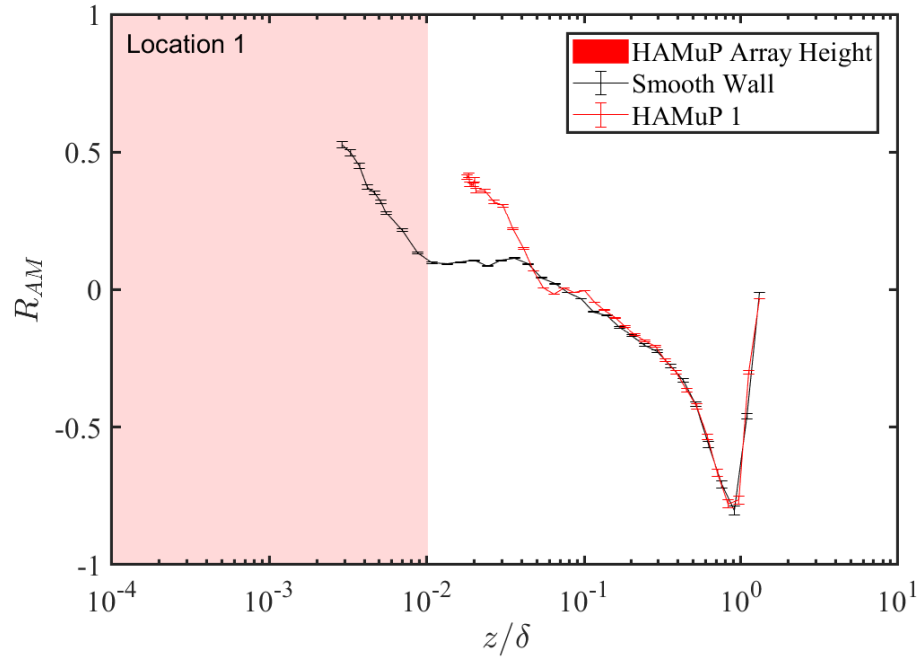


*Figure 4.5* The figure shows the amplitude modulation coefficient ( $R_{AM}$ ) for HAMuP array 1 in comparison with a smooth wall. The red region represents the approximate height of the HAMuP array.

flows over the HAMuP array. This suggests a shift in the viscous sub-layer away from the wall. This is an important result as past studies have shown that (Fukagata et al., 2002) Reynold's stress within 80 wall units from the wall is responsible for 90% of turbulent contribution to the skin friction. Previous researchers (Choi, Moin, & Kim, 1994) have targeted the near-wall cycle to achieve drag reduction.

Considering the energy spectra, the energy is redistributed from large scales to small scales with the most energetic structures pushed further away from the wall. It is hypothesized that the large scale structures are damped by the action of micro-pillars. The shift of the energetic structures to smaller scales can be attributed to the wake shed by the micro-pillars. The  $R_{AM}$  profile provides an interesting insight into the possible sensory applications for HAMuP arrays.

To get a more complete sense of the impact of the HAMuP array, two locations behind the array were surveyed using a hot-wire (Figure 4.1). Figure 4.6 shows the mean velocity profile just behind the HAMuP array(location 2). A velocity deficit is observed from

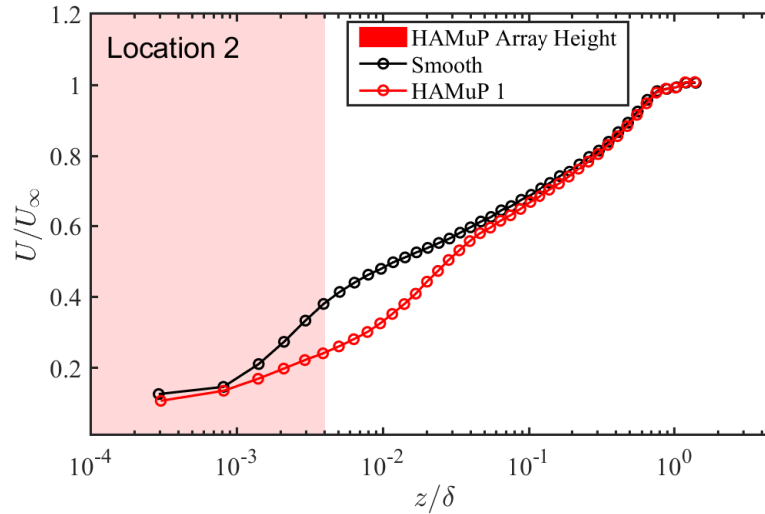


*Figure 4.6* The figure shows the mean velocity profile for HAMuP array 1 in comparison with the smooth wall at location 2. The red region represents the approximate height of the HAMuP array.

$z/\delta = 2 \times 10^{-3}$  to  $z/\delta = 5 \times 10^{-2}$  which agrees with the hot-wire measurements over the HAMuP array at location 1. Again, the velocity profiles for both smooth and HAMuP array 1 collapse in the outer region

Turbulent-intensity profiles also exhibit similar trends as seen at location 1 (see Figure 4.7). The turbulence intensity peak for HAMuP array is shifted away from the wall as compared with the smooth wall. The shift is accompanied by a slight increase in the magnitude of the turbulence intensity for the HAMuP array. The scale decomposition provides further details about the changes to the flow. There is a shift in the small scale intensity peak also accompanied with a slight increase in comparison to smooth wall. The large scale intensity in the near wall region is reduced for the HAMuP array when compared with the smooth wall. The largest reduction is observed at wall normal locations corresponding to the height of micro-pillars. The energy spectra of flows behind the HAMuP array are compared in figure 4.8. The energy spectra shows that the distribution of the most energetic structures is again skewed towards the smaller scales when compared with the spectra for smooth flow. Also, there is a shift in the most energetic structures away from the wall.

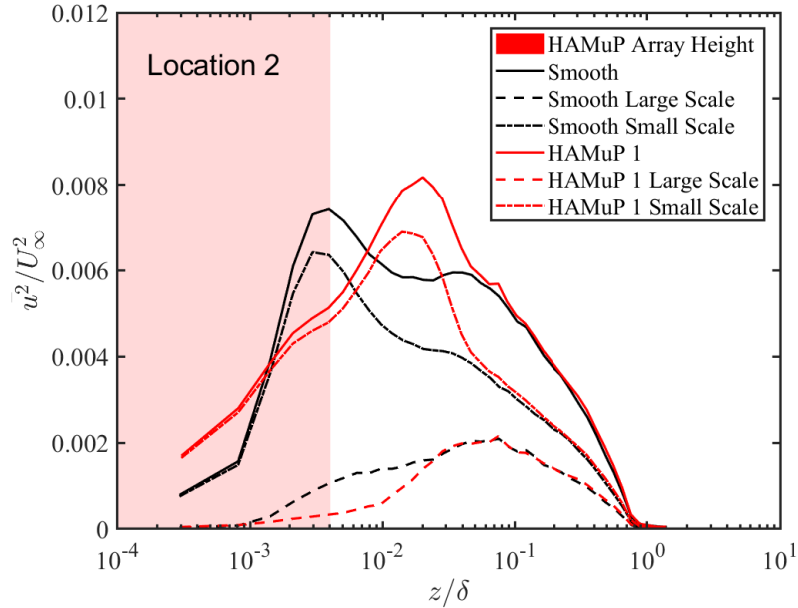


*Figure 4.7* The turbulent intensity profiles for HAMuP 1 and smooth wall at location 2 are shown here. The scale decomposition is also presented. The red region represents the approximate height of the HAMuP array.

Looking at the amplitude modulation profile again enforces the agreement of the data taken at both the locations 1 and 2 (Figure 4.7). The  $R_{AM}$  is again higher for the HAMuP array in the near-wall region while the profiles collapse in the outer region. The presence of micro-pillar wake is the likely reason for the increase in turbulence intensity. Regardless of this increase, the viscous sub-layer moved further away from the wall, similar to location 1. The skewed distribution of energy among small scales is also a recurring observation. Similar to the turbulent-intensity profiles, the most energetic structures are also shifted away from the wall. This can again be attributed to the presence of micro-pillar wake.

Measurements were conducted at location 3 to ascertain if the effects of the HAMuP array persist downstream of the array. Figure 4.9(a) shows the mean velocity profile 1 inch behind the HAMuP array (location 3). The mean velocity deficit, as observed at locations 1 and 2 in the near wall region, is greatly reduced but not completely eliminated. The turbulence intensity profile reveals a shift in the turbulence intensity peaks and a slight reduction of the turbulence intensity for the flow over the HAMuP array when

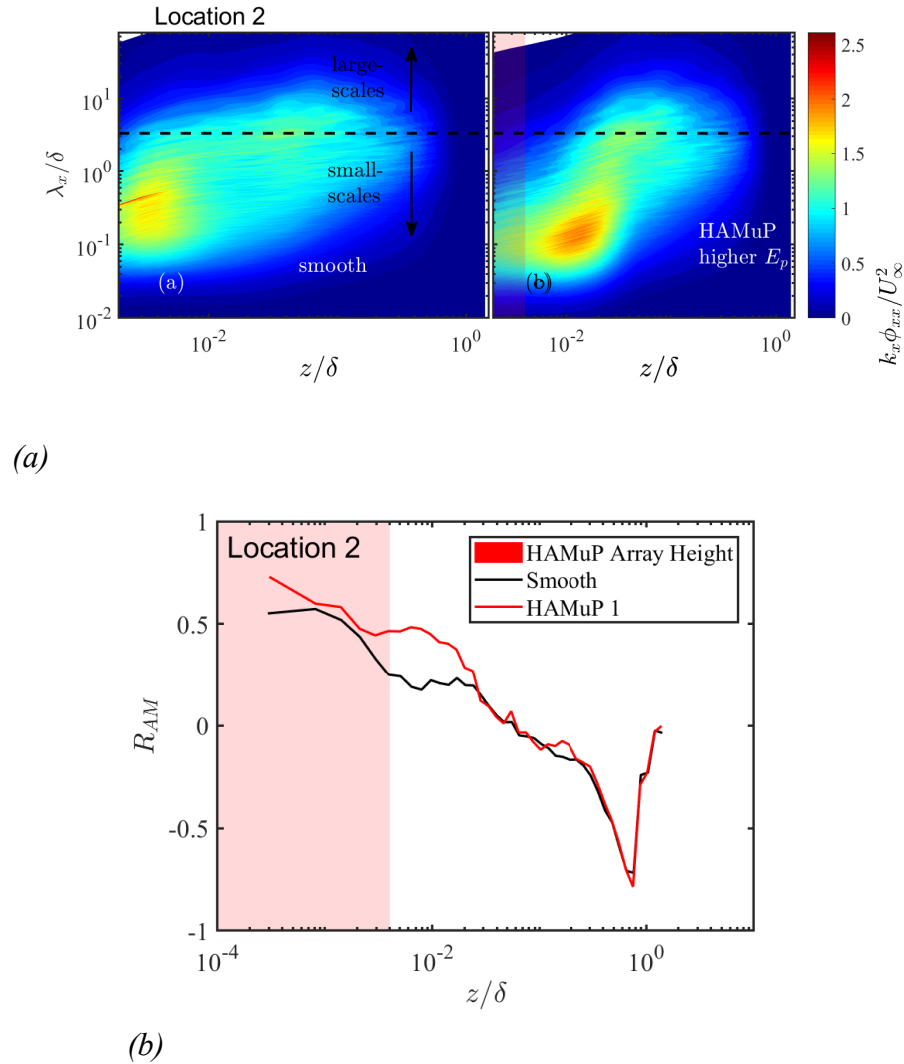


*Figure 4.8* (a) The figure here presents the outer normalized, pre-multiplied, 1-d streamwise energy spectra,  $k_x \phi_{xx}$ , for smooth wall and the HAMuP 1 at location 2. The dotted line is the division between large scale and small scales. The red region represents the average height of the HAMuP array. (b)  $R_{AM}$  profiles for HAMuP 1 and smooth wall at location 2.

compared with a smooth wall (Figure 4.9(b)). The turbulent intensity profile is decomposed into its large scale and small scale components. Similar to behavior seen at location 1 and 2, the small scale peak in the inner region is shifted away for the HAMuP array in comparison to the smooth wall. On the other hand, the large scale turbulent-intensity profiles collapse on each other.

The energy spectra provides an interesting insight into the effect of the HAMuP array

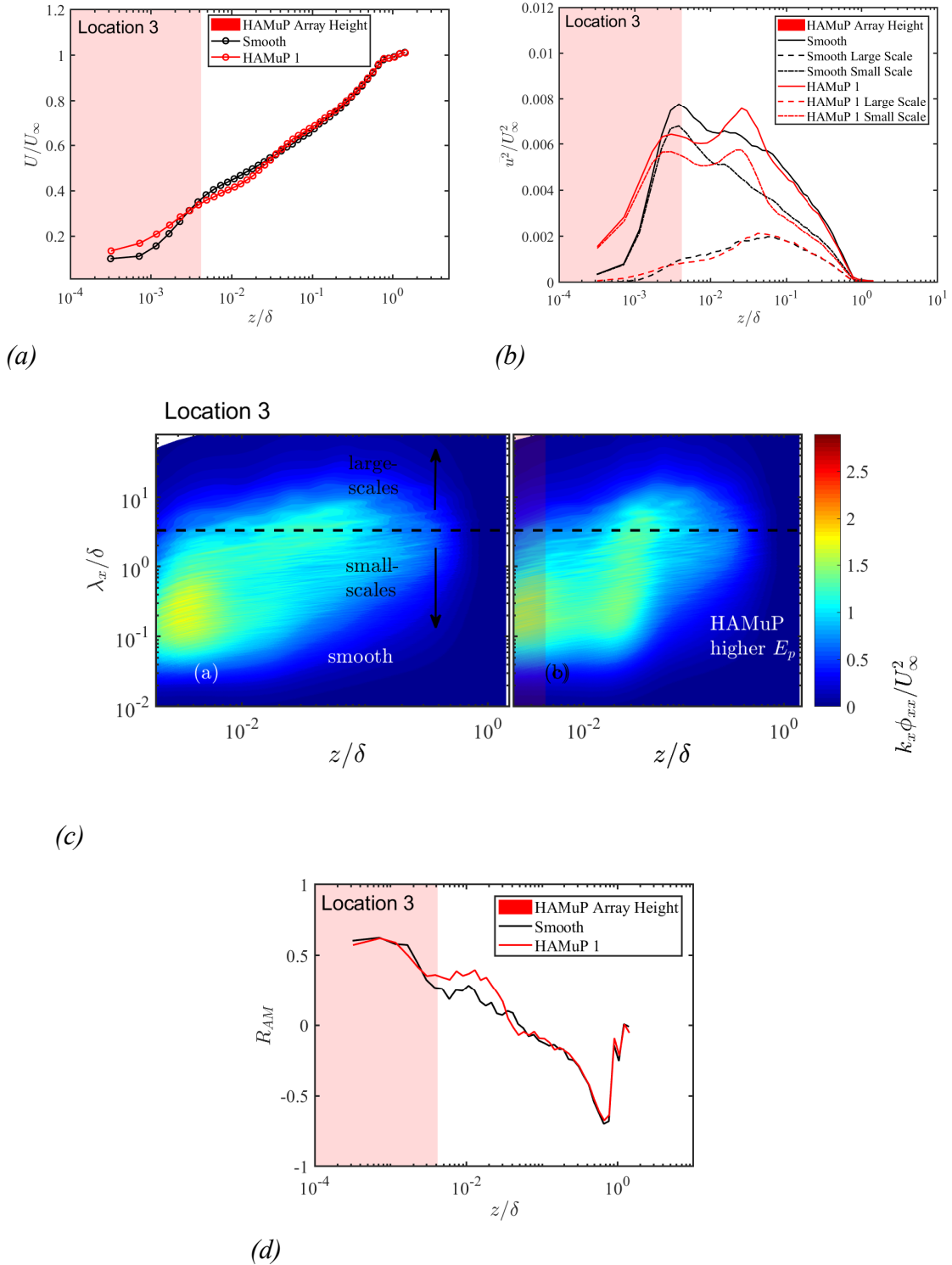


Figure 4.9 (a) Mean velocity profile downstream of the HAMuP array (location 3). (b) Turbulent intensity profiles for HAMuP array at location 3. (c) The figure here presents the outer normalized, pre-multiplied, 1-d streamwise energy spectra,  $k_x \phi_{uuu}$ , for smooth wall and the micro-pillar array at location 3. The dotted line is the division between large scale and small scales. (d)  $R_{AM}$  profiles for HAMuP 1 and smooth wall at location 3.

downstream of the array(see Figure 4.9(c)). The energy is redistributed towards the smaller scales of the flow with HAMuP array. More importantly though, the energy of the most energetic structures is considerably lower when compared with the smooth wall flow. The presence of HAMuP array appears to dampen the most energetic structures in the flow. The increase in  $R_{AM}$  in the near wall region persists downstream of the HAMuP array though the increase is reduced (Figure 4.9(d)).

The effects of HAMuP array seems to propagate downstream of the array, visible in data taken 1 inch (approximately  $9-10\delta$ ) behind the HAMuP array. The shift in viscous sub-layer is still observed. The energy spectra reveals that the HAMuP array appears to dampen the energetic structures in the near wall region. It is hypothesized that this energy is transferred as elastic deformation to the HAMuP array. This agrees with the findings of Toloui et al. (2019). Study of the  $R_{AM}$  profiles show an increase in the amplitude modulation coefficient of the flow downstream of the HAMuP array.

The impact of HAMuP array depends of multiple parameters like the height of the micro-pillars, their radius, the array spacing, etc. Two parameters, elastic modulus and the height of the micro-pillars, were selected for the purposes of a parametric study.

#### 4.2. Effect of Change in Elastic Modulus on HAMuP Performance

To understand the effect of elastic modulus on HAMuP performance, the micro-pillars are assumed to be cantilevers under uniformly distributed load. The deflection of a cantilever under uniformly distributed load is given by:

$$\delta = \frac{wL^4}{8EI} \quad (4.2)$$

where  $\delta$  is the deflection of the beam,  $w$  is the uniformly distributed load,  $L$  is the length of the beam,  $E$  is the Young's Modulus and  $I$  is the moment of inertia of the beam. The term  $EI$  is also known as the flexural rigidity of the beam. Flexural rigidity defines the resistance of a beam to deformation under a given load.

Elastic energy is the potential energy stored in a beam due to its deformation. The

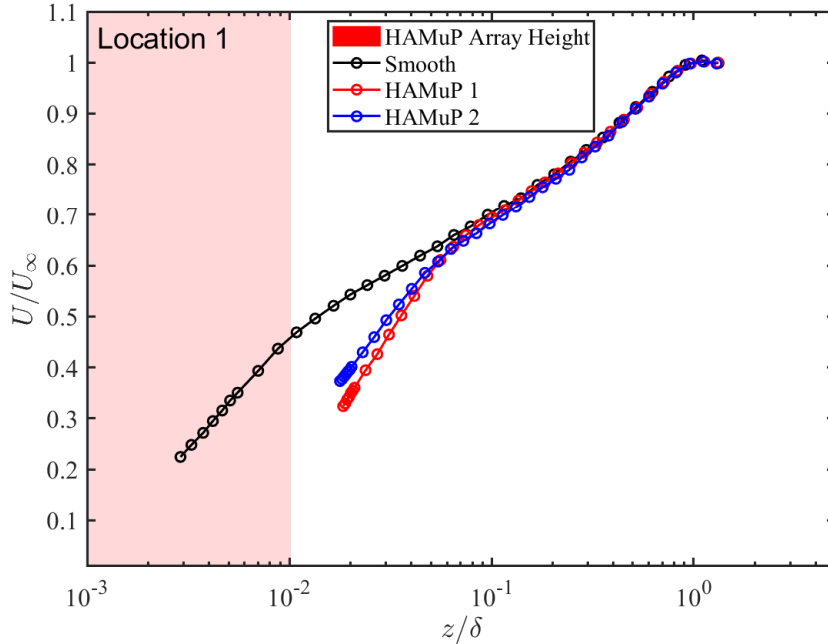


*Figure 4.10* The mean velocity profile of HAMuP array 1 and 2 along with the velocity profile over a smooth wall at location 1. The red region represents the approximate height of the HAMuP array.

equation below gives the elastic energy stored in a beam:

$$U = \frac{M^2 L}{2EI} \quad (4.3)$$

where  $M$  is the bending moment,  $L$  is the length of the beam and  $U$  is the elastic bending energy of the beam. The elastic energy that can be stored in a beam is inversely dependent on the the flexural rigidity while the flexural rigidity is directly dependent on the Young's Modulus. Thus, beams with lower flexural rigidity can bend more while requiring less energy to achieve the same deflection as a beam with higher flexural rigidity.

To study the effect of the elastic modulus, an array (HAMuP array 2) was manufactured with the same geometrical parameters as array 1 but with a different elastic modulus. The elastic modulus was varied by decreasing the amount of hardener used with the resin by 20% when compared with the HAMuP array 1. The comparative results for the two HAMuP arrays are presented in this section.



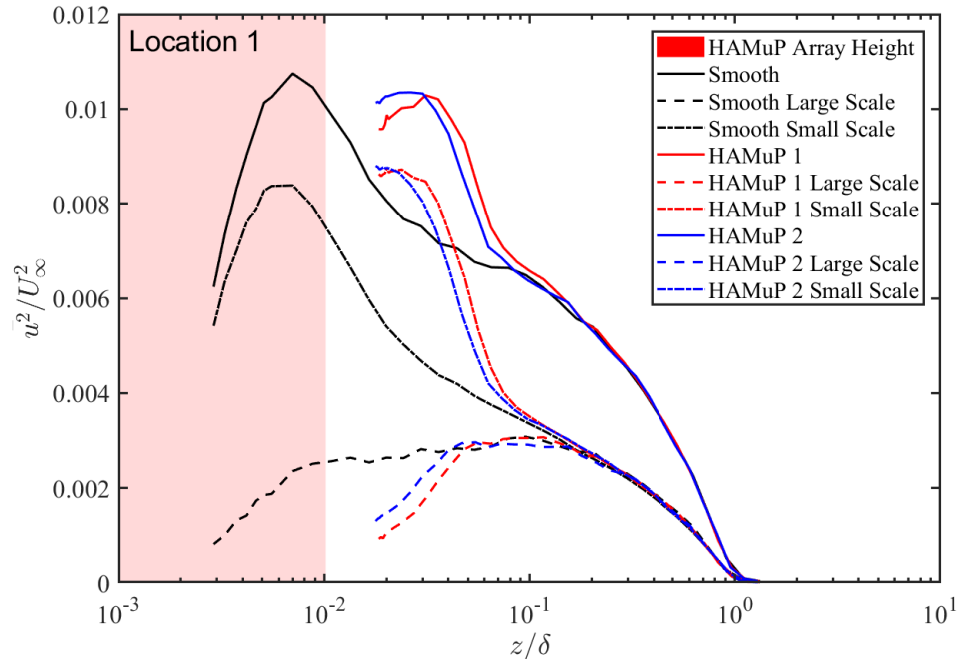


*Figure 4.11* The figure illustrates the turbulent intensity profiles for HAMuP array 1 and 2 in comparison with a smooth wall. Turbulence intensity for large and small scales in the flow is also shown. The red region represents the approximate height of the HAMuP array.

Figure 4.10 presents the mean velocity profile of the HAMuP array 1 and 2 at location 1. The velocity profile for the smooth surface is also presented for reference. The velocity deficit is slightly reduced in the near wall region for HAMuP 2 when compared with HAMuP 1. The difference is not very significant and both the HAMuP arrays exhibit larger deficits when compared with the smooth wall. For example, at  $z/\delta = 3 \times 10^{-2}$  the difference between HAMuP 1 and 2 is about 7% while it is about 25% between HAMuP 1 and the smooth wall.

Figure 4.11 presents the turbulence intensity profiles for HAMuP 1 and 2 at location 1. The profiles for HAMuP 1 and 2 show similar behavior with slight differences. The inner turbulence-intensity peak of flow over HAMuP 1 is shifted slightly more when compared with HAMuP 2. The HAMuP 1 peak is seen at  $z/\delta = 5 \times 10^{-2}$  while the HAMuP 2 peak is seen at  $z/\delta = 3 \times 10^{-2}$ .

The figure also presents the scale decomposition of the turbulent intensity profile. The marginal difference in the inner turbulent-intensity peaks is further seen in the shift of the

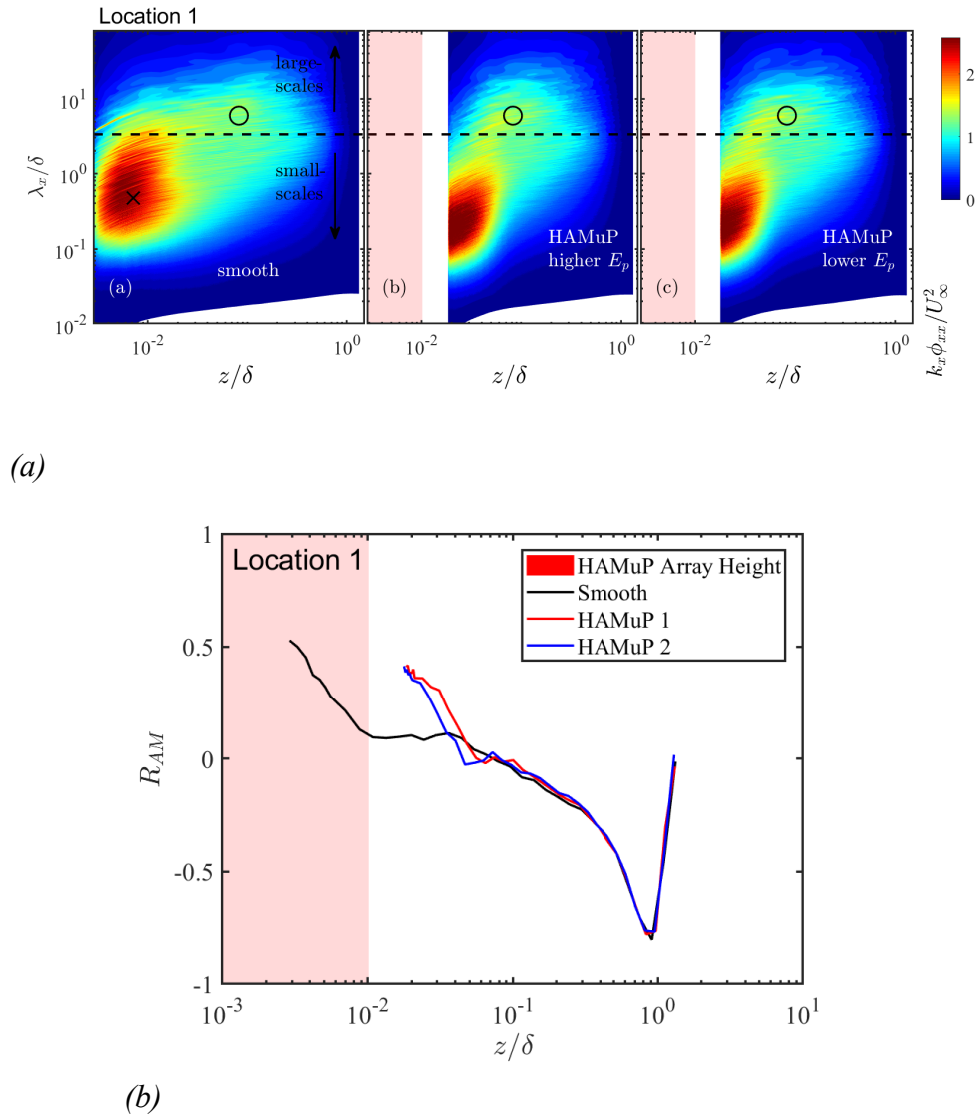


Figure 4.12 (a) The figure illustrates the outer normalized, pre-multiplied, 1-d streamwise energy spectra for HAMuP array 1 and 2 in comparison with a smooth wall at location 1. (b) The figure illustrates the  $R_{AM}$  profiles for HAMuP array 1 and 2 in comparison with a smooth wall at location 1. The red region represents the approximate height of the HAMuP array.

small scale peak. The large scale component of the turbulent-intensity is reduced for HAMuP 1 when compared with HAMuP 2. The energy spectra (Figure 4.12(a)) presents the outer normalized, pre-multiplied, 1-d streamwise energy spectra. HAMuP 1 and 2 both show a shift in energetic structures away from the wall. Also, a similar shift towards small structures is also observed for both. Figure 4.12(b) presents the  $R_{AM}$  profiles. Both

HAMuP 1 and 2 have higher amplitude modulation coefficients in the near wall region but the  $R_{AM}$  values for HAMuP 1 is marginally higher than HAMuP 2.

The reduction in Young's Modulus for array 2 resulted in a reduction in the flexural rigidity of its micro-pillars. Thus, the force required to deflect the micro-pillars in array 2 is lower than for those in array 1. As discussed before, it has been hypothesized that the HAMuP arrays convert the kinetic energy of the flow into bending or elastic energy. As less force is required to bend the micro-pillars of HAMuP array 2, they are able to extract slightly lesser energy from the flow. This could be a possible explanation for the slight change in the behavior of HAMuP 2 micro-pillars.

In the next section, the effect of micro-pillar height on the impact of HAMuP array on turbulent flow is investigated. The height of micro-pillars in HAMuP array 3 is  $735\mu\text{m}$  while it is  $600\mu\text{m}$  for HAMuP array 1 (see Table 4.1).

#### 4.3. Effect of Micro-Pillar Height on HAMuP Performance

Table 4.1

Table of parameters for different HAMuP arrays manufactured

Parameter	Array 1	Array 2	Array 3
Array Size	$55 \times 120$	$55 \times 120$	$55 \times 120$
Spacing (spanwise $\times$ streamwise)(mm)	$1 \times 0.5$	$1 \times 0.5$	$1 \times 0.5$
Pillar Height(mm)	0.6	0.6	0.735
Pillar Average Diameter(mm)	0.135	0.135	0.1
Resin-Hardener Ratio	1 : 1	1 : 0.8	1 : 1

The data for this comparison was taken at location 2, i.e., just behind the HAMuP arrays. Figure 4.13(a) presents the mean velocity profiles at location 2 of HAMuP array 1 and 3 with the velocity and wall normal distance normalized with respect to outer scaling parameters. The mean velocity profile for flow over smooth wall is also presented for reference.

The velocity deficit with respect to the smooth wall is reduced for HAMuP array 3 on comparison with array 1. The shift in turbulence intensity peak for HAMuP 3 is smaller

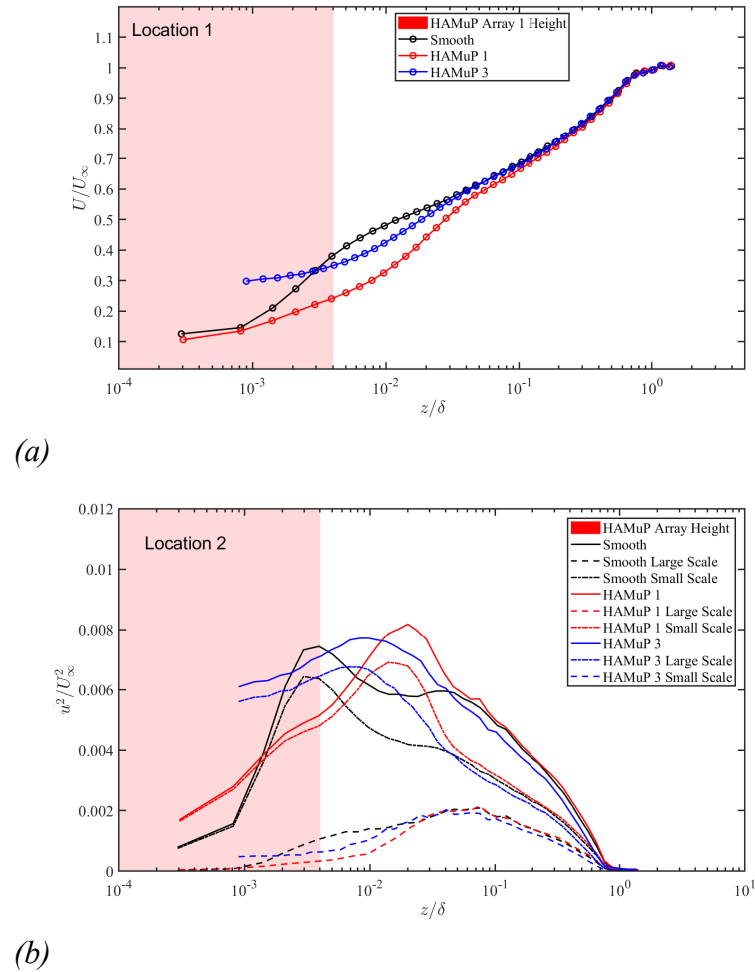
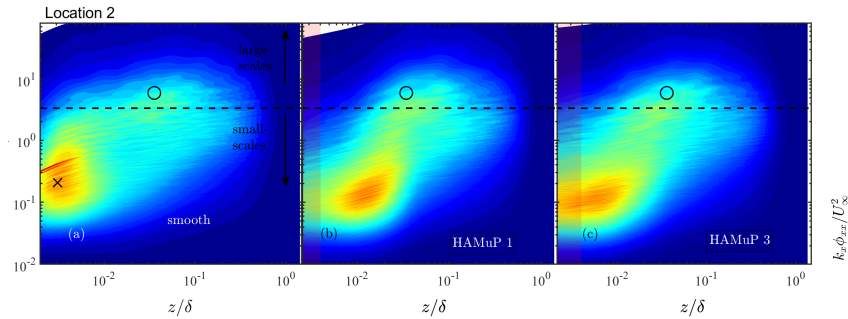
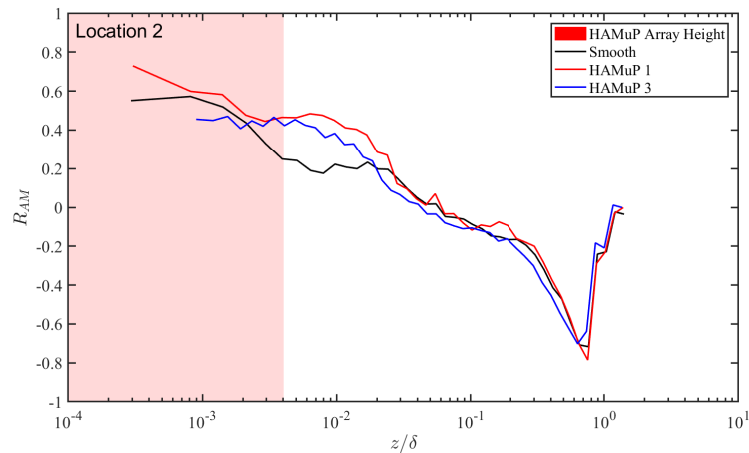


Figure 4.13 (a) The mean velocity profile for HAMuP array 1 and 3 is presented in comparison with a smooth wall at location 2. (b) The figure shows the turbulent-intensity profiles for HAMuP array 1 and 3 in comparison with a smooth wall. Turbulence-intensity for large and small scales in the flow is also shown. The red region presents the approximate height of HAMuP array 1.

(see Figure 4.13(b)) compared to HAMuP 1. The scale decomposition reveals a smaller shift in the small scales turbulent intensity for HAMuP 3. The flow over HAMuP 1 also experienced a larger reduction in the large scale intensity compared to HAMuP 3. The energy spectra (Figure 4.14(a)) provides further insight on the impact of height on the flow. The shift of the energetic structures away from the wall is smaller for HAMuP 3 when compared with HAMuP 1. Also, the presence of micro-pillar wake can be inferred from the increase in the energetic structures among the smaller scales for HAMuP 3. The  $R_{AM}$  for HAMuP 3 in the near wall region is also less than HAMuP 1 even though both the



(a)



(b)

Figure 4.14 (a) The figure presents the outer normalized, pre-multiplied, 1-d streamwise energy spectra at location 2., (b) The figure shows the amplitude modulation coefficient,  $R_{AM}$ , profiles for HAMuP 1 and 3. The red region represents the approximate height of HAMuP array 1.

arrays have higher amplitude modulation coefficients than the smooth wall (see Figure 4.14(b)).

Previous researchers (Brücker, 2011; Ptasinski et al., 2003) have targeted the near wall region of a turbulent wall bounded flow. According to a study by Iwamoto, Fukagata, Kasagi, and Suzuki (2005) damping the turbulence in the region with  $y^+ < 60$  will lead to maximum drag reduction. Although the study assumes perfect damping, it is a good indicator of the region of the flow to be targeted to get the best results. Increasing the height of the pillars might increase the potential elastic energy it can store but there is also an increase in the form drag due to the pillars.

## 5. Conclusion and Future Work

This work focuses on interaction of HAMuP array with wall turbulence. To facilitate this, a process was developed to manufacture consistent sets of HAMuP arrays. The interaction of these HAMuP arrays with wall-turbulence was studied using hot-wire anemometry. Velocity measurements were made at three different locations over the HAMuP array. A parametric study was conducted to identify the effects of different parameters on HAMuP performance. The parametric study was aimed at studying the effect of elastic modulus and height of micro-pillars on the HAMuP array performance, with the HAMuP array 1 as the baseline. The main conclusions to be drawn from the experimental results obtained are mentioned below:

1. The data taken at location 1 (over the HAMuP array) points towards a shift in the laminar sub-layer of the turbulent flow. The shift in turbulent intensity profile and the shift of energetic structures away from the wall lead to this conclusion. The energy is also redistributed towards smaller scales compared to the smooth wall.
2. The amplitude modulation coefficients is increased markedly in the near wall region of the flow over the HAMuP array. This increase could provide a possible explanation for the detection mechanism used by fishes to detect large scale motion.
3. The data taken behind the HAMuP array reveals the persistence of effects of HAMuP array on the wall turbulence. The effects are slightly muted but persist downstream of the flow. The shift in turbulent intensity profiles is still observed. The energy spectra illustrates the damping effect of the HAMuP array on the turbulent flow with a reduction in the energy of the most energetic structures.
4. HAMuP array 2, created with 20% less hardener as compared with HAMuP array 1, behaved similar to HAMuP array 1 with slight differences. The change in elastic modulus leads to a change in flexural rigidity of the micro-pillars. This is a possible explanation for the slight differences in the performance of HAMuP array 2. The reduction in flexural rigidity leads to a reduction of the energy required to achieve

the same deflection. As a result, the amount of energy the micro-pillars can extract from the flow is reduced.

5. Increase in height of the micro-pillars increases the micro-pillar wake and the drag caused by it. Previous researchers have targeted region in the near wall region with  $y^+ < 60$  to dampen the energetic structures in the flow. Increasing the height beyond the near wall region appears to be counter-productive with the drag increase outweighing the benefits of the elastic damping capacity of the tall micro-pillars.

This work has focused on understanding the effects of HAMuP array from a physics standpoint. The investigations done so far have been preliminary. Larger array are needed to obtain a more comprehensive picture of the HAMuP-wall turbulence interaction. Flow visualization would also reveal important details regarding this interaction and should be the focus of future work on HAMuP arrays. The  $R_{AM}$  profiles also indicate possible sensory applications that should be investigated in the future.

## REFERENCES

- Bechert, D., Bruse, M., W.Hage, & Meyer, R. (2000). Fluid mechanics of biological surfaces and their technological application. *Naturwissenschaften*.
- Bixler, G. D., & Bhushan, B. (2013). Fluid drag reduction with shark-skin riblet inspired microstructured surfaces. *Advanced Functional Materials*.
- Blackwelder, R. F., & Eckelmann, H. (1979). Streamwise vortices associated with the bursting phenomenon. *Journal of Fluid Mechanics*, 94, 577–594.
- Brücker, C. (2011, apr). Interaction of flexible surface hairs with near-wall turbulence. *Journal of Physics: Condensed Matter*, 23(18), 184120.
- Chen, H., Rao, F., Shang, X., Zhang, D., & Hagiwara, I. (2014, 02). Flow over bio-inspired 3d herringbone wall riblets. *Experiments in Fluids*, 55.
- Choi, H., Moin, P., & Kim, J. (1994). Active turbulence control for drag reduction in wall-bounded flows. *Journal of Fluid Mechanics*, 262, 75–110.
- Fukagata, K., Iwamoto, K., & Kasagi, N. (2002, 11). Contribution of reynolds stress distribution to the skin friction in wall-bounded flows. *Physics of Fluids - PHYS FLUIDS*, 14.
- Grbl:about*. (2017). Retrieved from <https://github.com/gnea/grbl/wiki>
- Iwamoto, K., Fukagata, K., Kasagi, N., & Suzuki, Y. (2005). Friction drag reduction achievable by near-wall turbulence manipulation at high reynolds numbers. *Physics of Fluids*, 17(1), 011702-011702-4.
- Jacobi, I., & McKeon, B. J. (2011). Dynamic roughness perturbation of a turbulent boundary layer. *Journal of Fluid Mechanics*, 688, 258–296.
- Jiménez, J. (2004, 01). Turbulent flows over rough wall. *Annu. Rev. Fluid Mech*, 36, 173-96.
- Jiménez, J., & Pinelli, A. (1999). The autonomous cycle of near-wall turbulence. *Journal of Fluid Mechanics*, 389, 335–359.
- Kline, S., Reynolds, W., Schraub, F., & Runstadler, P. (1967, 12). The structure of turbulent boundary layer. *Journal of Fluid Mechanics*, 30, 741 - 773.
- Krogstad, P.-., Antonia, R. A., & Browne, L. W. B. (1992). Comparison between rough- and smooth-wall turbulent boundary layers. *Journal of Fluid Mechanics*, 245, 599–617.
- Makris, C., Memos, C., & Krestenitis, Y. (2016, 02). Numerical modeling of surf zone dynamics under weakly plunging breakers with sph method. *Ocean Modelling*, 98, 12-35.



- Marshall, K. L., Chadha, M., deSouza, L. A., Sterbing-D'Angelo, S. J., Moss, C. F., & Lumpkin, E. A. (2015). Somatosensory substrates of flight control in bats. *Cell Reports*.
- Marusic, I., & Monty, J. (2019, 01). Attached eddy model of wall turbulence. *Annual Review of Fluid Mechanics*, 51.
- McKeon, B. J. (2017, Apr 25). The engine behind (wall) turbulence: perspectives on scale interactions. *Journal of Fluid Mechanics*, 817, 86.
- Mehta, D., Thota Radhakrishnan, A. K., & Clemens, F. (2018, 01). A wall boundary condition for the simulation of a turbulent non-newtonian domestic slurry in pipes. *Water*, 10, 124.
- Miller, G. (2005). Bats have a feel for flight. *Science*, 310(5752), 1260–1261.
- Monty, J., Chong, M., Mathis, R., Hutchins, N., Marusic, I., & Allen, J. (2010, 09). A high reynolds number turbulent boundary layer with regular ‘braille-type’ roughness. In *Iutam symposium on the physics of wall-bounded turbulent flows on rough walls* (Vol. 22, p. 69-75).
- Nakagawa, S., & Hanratty, T. J. (2001). Particle image velocimetry measurements of flow over a wavy wall. *Physics of Fluids*, 13(11), 3504-3507.
- Nikuradse, J., & Nikuradse, J. (1933). Laws of flow in rough pipes. *VDI Forschungsheft*, 361.
- Nugroho, B., Hutchins, N., & Monty, J. (2013, 06). Large-scale spanwise periodicity in a turbulent boundary layer induced by highly ordered and directional surface roughness. *International Journal of Heat and Fluid Flow*, 41, 90–102.
- Perry, A., Schofield, W., & Joubert, P. (1969, 06). Rough wall turbulent boundary layers. *Journal of Fluid Mechanics*, 37, 383 - 413.
- Perry, A. E., & Abell, C. J. (1977). Asymptotic similarity of turbulence structures in smooth- and rough-walled pipes. *Journal of Fluid Mechanics*, 79, 785–799.
- Ptasinski, P. K., Boersma, B. J., Nieuwstadt, F. T. M., Hulsen, M. A., Van Den Brule, B., & Hunt, J. C. R. (2003, 09). Turbulent channel flow near maximum drag reduction: simulations, experiments and mechanisms. *Journal of Fluid Mechanics*, 490, 251-291.
- Sabot, J., Saleh, I., & Comte-Bellot, G. (1977). Effects of roughness on the intermittent maintenance of reynolds shear stress in pipe flow. *The Physics of Fluids*, 20(10), S150-S155.
- Smith, C., Walker, J., Haidari, A., & Sobrun, U. (1991, 08). On the dynamics of near-wall turbulence. *Philosophical Transactions of The Royal Society B: Biological Sciences*,

336, 131-175.

- Smits, A. J., & Marusic, I. (2013). Wall-bounded turbulence. *Physics Today*, 66(9), 25-30.
- Squire, D., Baars, W., Hutchins, N., & Marusic, I. (2016, 09). Inner–outer interactions in rough-wall turbulence. *Journal of Turbulence*, 1-20.
- Sridhar, A., Pullin, D., & Cheng, W. (2017, 05). Rough-wall turbulent boundary layers with constant skin friction. *Journal of Fluid Mechanics*, 818, 26-45.
- Swearingen, J. D., & Blackwelder, R. F. (1987). The growth and breakdown of streamwise vortices in the presence of a wall. *Journal of Fluid Mechanics*, 182, 255–290.
- Tao, J., & Yu, X. B. (2012). Hair flow sensors: from bio-inspiration to bio-mimicking a review. *Smart Materials and Structures*.
- Toloui, M., Abraham, A., & Hong, J. (2019). Experimental investigation of turbulent flow over surfaces of rigid and flexible roughness. *Experimental Thermal and Fluid Science*, 101, 263 - 275.
- Townsend, A. (1956). *The structure of turbulent shear flow*.
- Vishwanath, P. (2002). Aircraft viscous drag reduction using riblets. *Progress in Aerospace Sciences*.
- Winzen, A., Klaas, M., & Schröder, W. (2013, 08). High-speed piv measurements of the near-wall flow field over hairy surfaces. *Experiments in Fluids*, 54, 1472.